Increased dosage of DYRK1A leads to congenital heart defects in a mouse model of Down syndrome

Eva Lana-Elola, Rifdat Aoidi, Miriam Llorian, Dorota Gibbins, Callan Buechsenschuetz, Claudio Bussi, Helen Flynn, Tegan Gilmore, Sheona Watson-Scales, Marie Haugsten Hansen, et al.

To cite this version:

Eva Lana-Elola, Rifdat Aoidi, Miriam Llorian, Dorota Gibbins, Callan Buechsenschuetz, et al.. Increased dosage of DYRK1A leads to congenital heart defects in a mouse model of Down syndrome. Science Translational Medicine, 2024, 16 (731), pp.eadd6883. 10.1126/scitranslmed.add6883 . hal-04747430

Increased dosage of DYRK1A leads to congenital heart defects in a mouse model of Down syndrome

Authors:
Eva Lana-Elola[1§], Rifdat Aoidi[1§], Miriam Llorian[1], Dorota Gibbins[1], Callan Buechsenschuetz[1], Claudio Bussi[1], Helen Flynn[1], Tegan Gilmore[1], Sheona Watson-Scales[1], Marie Haugsten Hansen[1], Darryl Hayward[1], Ok-Ryul Song[1], Véronique Brault[2], Yann Herault[2], Emmanuel Deau[3], Laurent Meijer[3], Ambrosius P. Snijders[1], Maximiliano G. Gutierrez[1], Elizabeth M. C. Fisher[4]*, Victor L. J. Tybulewicz[1]*

Affiliations:
[1]The Francis Crick Institute, London, NW1 1AT, UK
[2]Université de Strasbourg, CNRS UMR7104, INSERM U1258, Institut de Génétique et de Biologie Moléculaire et Cellulaire, IGBMC, BP 10142, 1 rue Laurent Fries, 67404 Illkirch CEDEX, France
[3]Perha Pharmaceuticals, Presqu'île de Perharidy, 29680 Roscoff, France
[4]Department of Neuromuscular Diseases, UCL Institute of Neurology, London, WC1N 3BG, UK

[§]These authors contributed equally

Corresponding author Emails: Victor.T@crick.ac.uk; elizabeth.fisher@ucl.ac.uk

OVERLINE: Down syndrome

One Sentence Summary:
Increased DYRK1A dosage in the Dp1Tyb mouse model of Down syndrome causes mitochondrial dysfunction and congenital heart defects.

Abstract

Down syndrome (DS) is caused by trisomy of human chromosome 21 (Hsa21). DS is a gene dosage disorder that results in multiple phenotypes including congenital heart defects. This clinically important pathology is the result of a third copy of one or more of the approximately 230 genes on human chromosome 21, but the identity of the causative dosage-sensitive genes and hence mechanisms underlying this cardiac pathology remain unclear. Here, we show that hearts from human fetuses with DS and embryonic hearts from the Dp1Tyb mouse model of DS show reduced expression of mitochondrial respiration genes and cell proliferation genes. Using systematic genetic mapping, we determined that three copies of the *dual-specificity tyrosine phosphorylation-regulated kinase 1A* (*Dyrk1a*) gene, encoding a serine/threonine protein kinase, are associated with congenital heart disease pathology. In embryos from the Dp1Tyb DS mouse model, reducing *Dyrk1a* copy number from three to two, reversed defects in cellular proliferation and mitochondrial respiration in cardiomyocytes and rescued heart septation defects. Increased dosage of DYRK1A results in impairment of mitochondrial function and congenital heart disease pathology in mice with DS, suggesting that DYRK1A may be a useful therapeutic target for treating this common human condition.

Introduction

Down syndrome (DS), trisomy of human chromosome 21 (Hsa21), is a common human condition resulting in many different phenotypes, including learning and memory deficits, craniofacial alterations, early-onset Alzheimer's disease and congenital heart defects (CHD) (*1*). DS is a gene dosage disorder with an extra copy of one or more of the genes on Hsa21 resulting in the different phenotypes. However, the identities of these causative dosage-sensitive genes remain unclear (*1, 2*). Discovery of such causative genes would facilitate study of the pathological mechanisms, paving the way for therapies, which are lacking for most DS clinical conditions.

With an estimated prevalence of around 1 in 800 births, DS is the most common genetic cause of CHD, with around 50% of babies with DS presenting with cardiac defects at birth (*3, 4*). Typically, these are ventricular and atrioventricular septal defects (VSDs and AVSDs) and malformations of the outflow tract (*3-5*). The most severe defects, such as AVSDs, often require surgical intervention in the first years after birth, resulting in substantial morbidity and mortality (*6*). Several proteins encoded by Hsa21 genes have been proposed as candidates for CHD. These include DSCAM and JAM2 adhesion molecules, COL6A1, COL6A2 and COL18A1 collagens, ADAMTS1 and ADAMTS5 metallopeptidases, the DYRK1A kinase, RCAN1, an inhibitor of calcineurin phosphatase, and SYNJ1, a regulator of endosomes (*7*). However, there has been no direct genetic demonstration of causality for any of these genes in studies that modulate gene dosage from 3 to 2 (*2*). Hence pathological mechanisms underlying this clinically important condition are poorly understood.

Hsa21 is orthologous to three regions of the mouse genome on mouse chromosome 10 (Mmu10), Mmu16 and Mmu17, with the largest of these being on Mmu16 (*2*). In previous work we generated the Dp1Tyb mouse model of DS that has an extra copy of the entire 23 Mb Hsa21-orthologous region of Mmu16 containing 145 coding genes in a tandem duplication, thereby genetically recapitulating trisomy of around 62% of Hsa21 genes (*8*). Dp1Tyb mice have a broad range of DS-like phenotypes (*8, 9*). Importantly, these mice have CHD similar to those seen in humans with DS, with ~50% of embryonic day 14.5 (E14.5) Dp1Tyb embryos showing VSDs, AVSDs and outflow tract defects (*8*). Furthermore, making use of a series of mouse strains with an extra copy of shorter segments of the Hsa21-orthologous region of Mmu16, we were able to show that an extra copy of just 39 coding genes in Dp3Tyb mice is sufficient to cause CHD, and that this region must contain at least two causative genes (*8*).

Here we use transcriptomics of human DS fetal hearts and mouse embryonic hearts from the DS mouse models to show that reduced expression of mitochondrial respiration genes and cell proliferation genes correlates with CHD pathology. Using systematic genetic mapping we demonstrate that one of the causative genes for CHD in DS is *Dyrk1a*. We show that increased dosage of *Dyrk1a* results in impaired cell proliferation and mitochondrial respiration of cardiomyocytes and is necessary to cause CHD in DS.

Results

Embryonic hearts from human DS fetuses and mouse models of DS show transcriptomic similarities

To discover biochemical pathways that are altered in DS and contribute to the pathology of the cardiac defects, we used RNA sequencing (RNAseq) to analyze the transcriptome of human DS fetal hearts and age- and sex-matched euploid controls (table S1). Differential gene expression analysis showed that human DS hearts had upregulated expression of many Hsa21 genes (Fig. 1A, table S2). In addition, expression of a further

99 genes was significantly altered (*P*<0.05) and hierarchical clustering demonstrated that the transcriptomes of DS and euploid human fetal hearts were distinct (Fig. 1A, B).

To investigate further, we made use of the Dp1Tyb mouse model of DS, which has CHD similar to those seen in humans with DS (*8*). Focusing on embryonic day 13.5 (E13.5), which is the day before heart septation is completed, RNAseq analysis of Dp1Tyb and wildtype (WT) control mouse hearts showed that the genes present in three copies in Dp1Tyb mice were increased in expression by about 1.5-fold, as expected (Fig. 1C, fig. S1A, table S3). In addition, a further 243 genes showed altered expression in Dp1Tyb embryonic hearts, and hierarchical clustering showed that Dp1Tyb and WT mouse embryonic hearts were transcriptionally distinct (Fig. 1D). Gene set expression analysis (GSEA) (*10*) revealed significant changes (*P*<0.05) in multiple pathways in human DS and mouse Dp1Tyb embryonic hearts (Fig. 1E). Most of these pathways were altered in the same direction in both species, including decreased oxidative phosphorylation and cellular proliferation, and increased immune responses and epithelial to mesenchymal transition (EMT) compared to control subjects, showing that the transcriptional changes in Dp1Tyb mouse embryonic hearts resembled those in human DS hearts (Fig. 1E).

Decreased expression of oxidative phosphorylation and cell proliferation genes correlates with CHD

To identify which pathways were most likely to be involved in CHD pathogenesis, we extended the RNAseq analysis to two further mouse strains: Dp3Tyb and Ts1Rhr. Dp3Tyb embryos show CHD similar to those in Dp1Tyb mice and DS, but this strain has an extra copy of just 39 protein-coding genes. These genes are entirely contained within the large duplication in Dp1Tyb mice, thus demonstrating that these 39 genes are sufficient to cause CHD (Fig. 1F) (*8*). In contrast, Ts1Rhr embryos have an extra copy of a slightly shorter region containing just 31 genes and do not show CHD (*8*). Comparison of the transcriptional changes in Dp3Tyb and Ts1Rhr mouse embryonic hearts with those of mouse Dp1Tyb and human DS hearts, showed that the changes in DNA repair and protein secretion pathways were not seen in either Dp3Tyb or Ts1Rhr hearts and these were not considered further (Fig. 1G). Increased expression of immune response and EMT pathways was seen in both Dp3Tyb and Ts1Rhr hearts, demonstrating that these changes are not sufficient to cause CHD (Fig. 1G, tables S4 and S5). In contrast, decreased expression of oxidative phosphorylation genes correlated with CHD – it was seen in human DS fetal hearts, and in Dp1Tyb and Dp3Tyb mouse embryonic hearts, but not in Ts1Rhr mouse hearts (Fig. 1G, fig. S1B, C). Decreased expression of the 3 proliferation gene sets was seen in Dp3Tyb mouse hearts, but only 2 of these were also decreased in Ts1Rhr mouse hearts. These results suggest that impaired oxidative phosphorylation, and potentially cellular proliferation may contribute to the etiology of CHD.

scRNAseq reveals similar gene expression changes across different cell types in Dp1Tyb mouse embryonic hearts

Although RNAseq analysis identified dysregulated pathways, it was not able to specify which cell type was perturbed in Dp1Tyb hearts. To address this, we performed single cell RNAseq (scRNAseq) of WT and Dp1Tyb E13.5 mouse hearts and identified 14 clusters which were assigned to individual cell types based on expression of marker genes (Fig. 2A, B) (*11*). Many of the expected cell types were detected, including several sub-types of cardiomyocytes, endocardial cells, epicardial cells, fibroblasts, vascular endothelial cells, smooth muscle cells and macrophages (*11*). Comparison of the frequencies of each cell type showed that whereas all cell types were detected in each genotype (fig. S2), Dp1Tyb hearts had significantly reduced frequencies of ventricular and atrial cardiomyocytes and significantly increased frequencies of fibroblasts and vascular endothelial cells compared to WT hearts (*P*<0.05, Fig. 2C).

To determine which cell types showed the pathway changes seen in whole hearts, we subjected the scRNAseq data to GSEA. Initially, we pooled the scRNAseq across all cell types and found that this pseudo-bulk RNAseq analysis recapitulated the changes seen in the bulk RNAseq analysis, with Dp1Tyb mouse hearts showing decreased expression of oxidative phosphorylation and proliferation genes (Fig. 2D). Extending this analysis to the 11 most abundant cell clusters, we found that significantly decreased expression of the oxidative phosphorylation genes was seen in all cell types and significantly decreased expression of proliferation genes was seen in all cell types except epicardial cells, vascular endothelial cells, and atrioventricular cushion fibroblasts (*q*<0.05, Fig. 2D). Thus, decreased expression of oxidative phosphorylation and proliferation genes was seen across most cell types in Dp1Tyb mouse embryonic hearts.

Dp1Tyb mouse embryonic hearts show proliferative defects

Although the decreased cell proliferation signature was present in both human DS fetal hearts and mouse Dp1Tyb hearts, this change was insufficient to cause heart defect pathology since it was present in Ts1Rhr hearts which do not show CHD. To investigate directly if cell proliferation was affected in Dp1Tyb mouse embryonic hearts, we measured the fraction of cells in different cell cycle phases. Flow cytometric analysis of Dp1Tyb mouse hearts showed an increased proportion of cardiomyocytes and endocardial cells in G1, and fewer cells in S phase, consistent with impaired proliferation (Fig. 3A-B). This proliferation defect may explain the decreased fraction of cardiomyocytes in Dp1Tyb hearts.

Pathway analysis of human DS and Dp1Tyb mouse hearts showed downregulated E2F target genes in both species (Fig. 1E, G). The E2F transcription factors control the expression of genes required for the G1 to S phase transition of the cell cycle (*12*). Inspection of the genes in the 'leading edge' of the E2F target gene set in the GSEA showed that there were 72 and 153 downregulated genes in human DS fetal hearts and Dp1Tyb embryonic hearts respectively, with 49 genes downregulated in common between the two species, indicating that downregulation of E2F activity may be the cause of the impaired proliferation (table S6). The E2F factors are repressed by binding to the Retinoblastoma protein RB1 (*12*). Phosphorylation of RB1 by CDK4 and CDK6 kinases in complex with Cyclin D proteins leads to dissociation of RB1 from E2F proteins allowing the latter to activate genes required for the G1 to S phase transition (Fig. 3C). To examine if the reduced E2F activity in Dp1Tyb hearts was due to impaired phosphorylation of RB1, we used immunoblotting to quantify amounts of phosphorylated RB1 (p-RB1). We found that Dp1Tyb mouse hearts had significantly decreased p-RB1 ($P<0.05$), which may account for reduced E2F activity and hence impaired cell proliferation (Fig. 3D, E).

Dp1Tyb mouse embryonic cardiomyocytes have mitochondrial defects

To determine whether the decreased expression of oxidative phosphorylation genes indicated impaired mitochondrial respiration, we used flow cytometry to measure mitochondrial mass and the mitochondrial inner membrane potential of Dp1Tyb mouse hearts. Mitochondrial mass was not altered in either cardiomyocytes or endocardial cells, and mitochondrial potential was unchanged in endocardial cells, however, the ratio of cells with high to intermediate membrane potential was significantly reduced ($P<0.05$) in cardiomyocytes from E13.5 Dp1Tyb mouse hearts (Fig. 4A, B). Decreased mitochondrial membrane potential suggested that the maturation of Dp1Tyb mouse cardiomyocytes may be affected. A developmental transition, typically occurring at E11.5 in the mouse, is characterized by closure of the mitochondrial permeability transition pore, thereby elevating mitochondrial potential, and by elongation and branching of mitochondria (*13*). Confocal microscopy imaging showed that mitochondria in cardiomyocytes from Dp1Tyb mouse E13.5 hearts had significantly lower aspect ratios and form factors ($P<0.05$) compared to those in WT mouse cardiomyocytes, indicating that Dp1Tyb mitochondria are less elongated and branched, consistent with impaired cardiomyocyte maturation (Fig. 4C-D, fig. S3A-B). To directly analyze mitochondrial function, we measured mitochondrial respiration of Dp1Tyb mouse embryonic hearts. We found that cells from E13.5 Dp1Tyb mouse hearts had significantly reduced basal and maximal respiration rates ($P<0.05$), consistent with impaired mitochondrial function (Fig. 4E-F). Furthermore, analysis of glycolysis rates showed that cells from Dp1Tyb hearts had significantly increased rates of glycolysis ($P<0.05$), demonstrating a bioenergetic switch away from oxidative phosphorylation (Fig. 4G-H).

One possible cause for this switch towards glycolysis could be hypoxia, which through HIF-1α results in the upregulation of genes encoding enzymes in the glycolytic pathway (*14*). To investigate if increased hypoxia could be playing a role in this altered cardiac metabolism, we measured hypoxia in developing Dp1Tyb and control embryonic hearts by injecting pregnant mice with pimonidazole hydrochloride, also known as Hypoxyprobe (*15*). Pimonidazole covalently binds to thiol groups on proteins and amino acids in hypoxic cells and can be visualized with an antibody. This analysis showed no change in the amount of hypoxia in Dp1Tyb mouse hearts compared to WT mouse hearts (Fig. 4I-J). This result was further supported by GSEA which did not show any significant changes ($P>0.05$) in the expression of HIF-1α-regulated genes (table S6). Thus, increased hypoxia is unlikely to be the cause of the increased glycolysis. Taken together these results demonstrate that Dp1Tyb mouse embryonic hearts have impaired mitochondrial respiration, with a compensatory increase in glycolysis.

Three copies of *Dyrk1a* are necessary to cause heart defects

To gain further insight into the basis of CHD in DS we used systematic genetic mapping to identify a causative gene responsible for this pathology. Using a panel of mouse strains with a nested series of duplications of regions on Mmu16, we previously showed that a region of 39 genes duplicated in Dp3Tyb mice was sufficient to cause CHD (*8*). However, when this was broken down into three shorter duplicated regions in Dp4Tyb, Dp5Tyb and Dp6Tyb mice, none of the resulting strains had heart defects, implying that there must be at least two causative genes (Fig. 5A) (*8*). Furthermore, since Ts1Rhr mouse embryos do not have CHD, one of the causative genes must be within the 8 coding genes and 1 microRNA gene that are duplicated in Dp3Tyb but not Ts1Rhr mice (Fig. 5A). Another study showed that Dp(16)4Yey mice with an extra copy of a 35-gene region on Mmu16 which partially overlaps Dp3Tyb, also have CHD (*16*). This overlap includes 16 genes at the proximal end of the Dp3Tyb duplication covering the entire Dp4Tyb region and the first two genes within the Dp5Tyb region. Taken together, the simplest explanation for these results is that one causative gene lies within the proximal region duplicated in Dp3Tyb mice but not Ts1Rhr mice, containing two coding genes (*Setd4*, *Cbr1*) and a microRNA gene (*Mir802*) (Fig. 5A, orange), and a second causative gene lies within the first two genes of the Dp5Tyb region (*Dyrk1a*, *Kcnj6*) (Fig. 5A, blue). Thus, we tested the potential role for each of these 5 genes in causing CHD, by reducing its copy number in Dp1Tyb embryos from three to two.

We crossed Dp1Tyb mice to mouse strains deficient in each of the candidate genes, except for *Cbr1*, which we tested by crossing to Del4Tyb mice that have a deletion of the entire Dp4Tyb region (Fig. 5A, fig. S4A). For each cross we analyzed the hearts of E14.5 embryos using high resolution episcopic microscopy (HREM) (*17*) to generate detailed 3D images to accurately identify different types of CHD. As expected, compared to WT controls, Dp1Tyb embryos had increased rates of CHD, especially the more severe AVSD, which are typified by a common atrioventricular valve in place of separated mitral and tricuspid valves (Fig. 5B-H). Removing one copy of *Mir802*, *Setd4*, *Cbr1* or *Kcnj6* did not affect the frequency of CHD in general, or specifically AVSDs (Fig. 5B-E). However, reducing the copy number of *Dyrk1a* from three to two completely rescued CHD in Dp1Tyb*Dyrk1a*$^{+/+/-}$ mice (Fig. 5F, H). Thus, three copies of *Dyrk1a* are necessary to cause CHD in Dp1Tyb mice.

Dyrk1a encodes the DYRK1A serine/threonine protein kinase. To investigate whether increased DYRK1A kinase activity is required for CHD, we crossed Dp1Tyb mice to a strain carrying an allele coding for kinase-inactive DYRK1A (*Dyrk1a*$^{\mathrm{K188R}}$). The resulting Dp1Tyb*Dyrk1a*$^{+/+/\mathrm{K188R}}$ embryos had no increase in AVSDs compared to WT controls, and significantly fewer (P=0.0141) AVSDs than Dp1Tyb embryos (Fig. 5G-H). Thus, increased DYRK1A catalytic kinase activity is necessary for severe CHD in Dp1Tyb mice.

Increased dosage of *Dyrk1a* causes key transcriptional changes in Dp1Tyb embryonic hearts

Next, we investigated whether increased dosage of *Dyrk1a* was responsible for the transcriptional changes in Dp1Tyb mouse E13.5 embryonic hearts. A comparison of the transcriptomes of WT, Dp1Tyb and Dp1Tyb*Dyrk1a*$^{+/+/-}$ hearts showed that compared to WT controls, Dp1Tyb*Dyrk1a*$^{+/+/-}$ samples had increased expression of the duplicated genes, but very few other differentially expressed genes (Fig. 6A, table S7). In contrast, comparison of Dp1Tyb and Dp1Tyb*Dyrk1a*$^{+/+/-}$ mouse hearts showed large numbers of differentially expressed genes, as had been seen in the comparison of Dp1Tyb with WT controls (Fig. 6A). These results show that an extra copy of *Dyrk1a* was responsible for most of the transcriptional changes in developing Dp1Tyb mouse hearts. We extended this analysis to the proteome using mass spectrometric analysis of Dp1Tyb and Dp1Tyb*Dyrk1a*$^{+/+/-}$ mouse E13.5 hearts, revealing 290 differentially expressed proteins (Fig. 6B, table S8). As expected, the amount of DYRK1A was about 1.5-fold higher in Dp1Tyb compared to Dp1Tyb*Dyrk1a*$^{+/+/-}$ hearts. Moreover, pathway analysis of the transcriptomic and proteomic data showed that 3 copies of *Dyrk1a* are necessary for the decreased expression of oxidative phosphorylation and proliferation genes and increased expression of EMT genes, but not for the increased expression of immune response genes (Fig. 6C, fig. S1D, E). A comparison of the differentially expressed genes in Dp1Tyb versus WT mouse hearts and Dp1Tyb versus Dp1Tyb*Dyrk1a*$^{+/+/-}$ hearts, showed that there were 32 upregulated and 46 downregulated genes in common between these comparisons, representing genes most likely to be regulated by increased *Dyrk1a* dosage (table S9). STRING protein interaction (https://string-db.org/) analysis of these genes once again showed a clear signature of decreased networks of proteins involved in proliferation (table S9).

Furthermore, scRNAseq analysis of Dp1Tyb*Dyrk1a*$^{+/+/-}$ mouse E13.5 hearts showed that reduction of the copy number of *Dyrk1a* reversed the decreased fraction of cardiomyocytes and the increased fraction of fibroblasts seen in Dp1Tyb hearts (Fig. 2C, fig. S2), demonstrating that these changes in cell type abundance are dependent on three copies of *Dyrk1a*. Moreover, GSEA pathway analysis showed that changes in expression of oxidative phosphorylation, proliferation and EMT genes which were seen across most cell types, were also dependent on 3 copies *Dyrk1a* (Fig. 2D).

Dyrk1a is broadly expressed in many cardiac cell types

Since a third copy of *Dyrk1a* had a profound effect on the transcriptomes of most cell types in the developing heart, we examined its expression pattern. Using the scRNAseq data, we found that *Dyrk1a* was expressed in all cell types in E13.5 hearts, a conclusion that was further supported by RNAscope analysis of E12.5 and E14.5 hearts, an in situ hybridization method that detects mRNA in tissue sections (Fig. 7A-B). This broad expression of *Dyrk1a* is consistent with a role for increased DYRK1A causing the observed pathway changes across multiple cell types.

Increased dosage of *Dyrk1a* is necessary for reduced proliferation in Dp1Tyb mouse embryonic hearts

Next, we investigated whether increased dosage of *Dyrk1a* was also required for the physiological changes seen in Dp1Tyb mouse embryonic hearts. Analysis of proliferation showed that Dp1Tyb*Dyrk1a*$^{+/+/-}$ mouse cardiomyocytes and endocardial cells had no change in the fraction of cells in G1, S and G2/M phases compared to WT cells, demonstrating that 3 copies of *Dyrk1a* were necessary for the impaired proliferation (Fig. 3A, B). Furthermore, the reduction in phosphorylated RB1 in Dp1Tyb mouse embryonic hearts was also reversed by reducing the copy number of *Dyrk1a* from 3 to 2 (Fig. 3D-E), and Dp1Tyb*Dyrk1a*$^{+/+/-}$ hearts no longer showed reduced expression of E2F target genes (Fig. 6C, table S6).

Increased expression of DYRK1A may cause decreased cell proliferation by phosphorylating Cyclin D (CCND) proteins, leading to their degradation (Fig. 3C) (*18-22*). To investigate whether this was occurring in Dp1Tyb mouse hearts we used mass spectrometry to compare the phospho-proteomes of Dp1Tyb and Dp1Tyb*Dyrk1a*$^{+/+/-}$ E13.5 hearts, showing that there were many phospho-peptides whose abundance differed significantly ($P<0.05$) because of a third copy of *Dyrk1a* (Fig. 6B, table S8). This included increased pS520-DYRK1A, an autophosphorylation site of the kinase, consistent with increased DYRK1A activity in Dp1Tyb compared to Dp1Tyb*Dyrk1a*$^{+/+/-}$ hearts (*23*). However, we saw no change in the abundance of pT280-CCND2, a site reported to be phosphorylated by DYRK1A in cardiomyocytes (Fig. 6B) (*20*). Furthermore, we were able to detect only two other known DYRK1A phosphorylation targets, pS10-CDKN1B and pS557-CRY2, neither of which was altered in abundance. However, analysis of the whole proteome showed a decreased abundance of CCND2 in Dp1Tyb hearts ($P<0.05$), and decreased abundance of CCND1 and CCND3, though these latter changes were not significant ($P>0.05$) (Fig. 6B). These results are consistent with increased dosage of DYRK1A impairing proliferation in Dp1Tyb embryonic hearts through phosphorylation and subsequent degradation of CCND2, leading to reduced CDK4/6-induced phosphorylation of RB1 and hence less expression of E2F-regulated genes that are required for G1 to S phase transition.

Three copies of *Dyrk1a* cause mitochondrial dysfunction in embryonic cardiomyocytes

Next, we examined whether the mitochondrial dysfunction in Dp1Tyb mouse cardiomyocytes was dependent on 3 copies of *Dyrk1a*. We found that reduction of the copy number of *Dyrk1a* from 3 to 2 reversed the decreased mitochondrial potential and impaired mitochondrial morphology in Dp1Tyb mouse cardiomyocytes (Fig. 4A-D). Furthermore, cells from Dp1Tyb*Dyrk1a*$^{+/+/-}$ mouse E13.5 hearts showed normal rates of basal and maximal respiration and glycolysis (Fig. 4E-H).

Pharmacological inhibition of DYRK1A results in a partial reversal of transcriptional changes in Dp1Tyb mouse embryos

Finally, we investigated whether treatment of pregnant mice with an inhibitor of DYRK1A kinase activity could reverse the CHD in Dp1Tyb mouse embryos. To investigate this we used Leucettinib-21, a recently developed DYRK1A inhibitor and a negative control, iso-Leucettinib-21, an inactive isomer (fig. S5A). Leucettinib-21 is a potent inhibitor of DYRK1A (IC_{50} = 3.1 nM), whereas iso-Leucettinib-21 has an IC_{50} >10 μM for DYRK1A (*24*). First, we asked if Leucettinib-21 administered to the pregnant mouse could pass through the placenta into the embryo. Analysis of mice treated with 0.3, 3 or 30 mg/kg of Leucettinib-21 showed detectable Leucettinib-21 in the embryo at 3 and 30 but not 0.3 mg/kg (Fig. S5B). Based on the measured amounts of Leucettinib-21 in the embryo, the 3 and 30 mg/kg doses resulted in around 24 nM and 560 nM Leucettinib-21 in the embryo. We chose to use 30 mg/kg Leucettinib-21 to maximize the chance of observing an effect.

We treated pregnant mice with Leucettinib-21 or iso-Leucettinib-21 daily starting at E5.5, which is before the heart forms, until E13.5 for RNAseq analysis and E14.5 for analysis of CHD by HREM (Fig. 8A). Homozygous genetic deletion of *Dyrk1a* results in a mid-gestation lethality, with no embryos surviving beyond E13.5 (*25*). Thus, it was possible that Leucettinib-21 treatment would cause embryonic lethality. However, we found that treatment of mated mice with 30 mg/kg Leucettinib-21 did not affect the fraction of mice that became pregnant or the size of their litters (fig. S5C-D). Furthermore, the recovery of Dp1Tyb embryos at E14.5 was also not affected (fig. S5E), in line with the normal segregation of the mutation, as previously reported (*8*). Thus, Leucettinib-21 treatment does not interfere with pregnancy and is likely only partially inhibiting DYRK1A.

RNAseq analysis of E13.5 embryos from mice treated with Leucettinib-21 or iso-Leucettinib-21 showed that the active Leucettinib-21 inhibitor partially reversed the decreased expression of genes in the oxidative phosphorylation and proliferation (Myc targets v1) pathways in Dp1Tyb embryonic hearts, however, it had no effect on the increased expression of inflammatory genes in the mutant hearts (Fig. 8B, table S10). The changes in expression caused by Leucettinib-21 were qualitatively similar to the changes seen when the copy number of *Dyrk1a* was reduced from 3 to 2 in Dp1Tyb embryos but were smaller in magnitude, consistent with Leucettinib-21 causing a partial inhibition of DYRK1A in the embryonic heart (Fig. 8C). Lastly, we used HREM to analyze the embryos for CHD. We found that Leucettinib-21 treatment resulted in a frequency of CHD in Dp1Tyb embryos that was between that seen in WT and Dp1Tyb embryos treated with iso-Leucettinib-21, but was not significantly different from either (P>0.05) (Fig. 8D). This is consistent with the possibility that inhibition of DYRK1A results in a partial rescue of the DYRK1A-dependent CHD in Dp1Tyb embryos but more work would be required to establish this.

Discussion

Here we show that heart tissue from human fetuses with DS have characteristic transcriptional changes, many of which are shared with embryonic hearts from the Dp1Tyb and Dp3Tyb mouse models of DS that show CHD. Gene set enrichment analysis identified several pathways that were altered in the hearts of both human DS and mouse models. Of these, decreased expression of oxidative phosphorylation genes correlated most strongly with CHD in the mouse models, suggesting that impaired mitochondrial function may be an important cause of the developmental defects. In agreement with our results, decreased expression of oxidative phosphorylation genes in human DS fetal hearts has been previously seen using microarray technology (*26*). In addition, physiological analysis demonstrated reduced mitochondrial membrane potential and respiration in Dp1Tyb mouse embryonic cardiomyocytes. Decreased expression of proliferation genes partially correlated with CHD, being seen in human DS hearts, and mouse Dp1Tyb and Dp3Tyb hearts. Hearts from the Ts1Rhr mouse strain which does not have CHD, also showed decreased expression of proliferation genes, but only in two out of three gene sets compared to a decrease in all three in Dp1Tyb and Dp3Tyb hearts, suggesting that impaired proliferation may also play an important role in CHD. Changes in several other pathways, such as increased expression of inflammatory, interferon response and EMT genes, were also seen in the human and mouse embryonic hearts. Since changes in these pathways were seen in hearts from Ts1Rhr mice, they are not sufficient on their own to cause heart defects. However, they may also contribute to CHD pathology, in combination with the mitochondrial and proliferative deficits.

It remains unclear how defects in mitochondrial function and proliferation in most cardiac cells can cause localized defects in septation, rather than a broader cardiomyopathy. One possibility is that the cellular changes are relatively small and that they preferentially affect structures involved in septation such as the ventricular septum, the atrioventricular and outflow tract cushions or the dorsal mesenchymal protrusion. Further work is needed to understand the developmental defects in Dp1Tyb mouse hearts that lead to VSD and AVSD.

Mitochondrial dysfunction has been previously reported in DS (*27-30*). Human DS fibroblasts, astrocytes and neurons have impaired mitochondrial respiratory activity, decreased mitochondrial membrane potential and altered mitochondrial shape with smaller and more fragmented mitochondria (*31-34*). This dysfunction may underlie the neurological and cognitive impairment in DS, contributing to decreased neurogenesis and altered processing of APP, leading to deposition of Aβ amyloid and early-onset Alzheimer's disease. Our results show that a very similar mitochondrial phenotype is evident in embryonic cardiomyocytes from the Dp1Tyb mouse model of DS and suggest that mitochondrial dysfunction may play an important role in the cardiac pathology in DS. This commonality of mitochondrial impairment across multiple DS tissues has led to the interesting proposal that drugs that increase mitochondrial biogenesis or respiratory capacity may be promising therapeutic candidates for DS phenotypes, for example, for cognitive deficits (*28-30*). Our results suggest that a similar approach may ameliorate cardiac defects.

We previously reported that Dp3Tyb mouse embryos have CHD, but Dp4Tyb, Dp5Tyb and Dp6Tyb mouse embryos do not, implying that there must be at least two causative genes whose increased dosage leads to CHD (*8*). Since we have now shown that the Dp4Tyb region is not required for CHD (Fig. 5D), the causative genes must lie in the regions duplicated in Dp5Tyb and Dp6Tyb mice, with at least one causative gene in each region (the 2-locus hypothesis, fig. S6). Whereas in this study we have identified *Dyrk1a* as a causative gene within the Dp5Tyb region, the second causative gene, referred to as *GeneX*, is likely to be one of the six coding genes present in three copies in Dp3Tyb and Dp6Tyb mice but not Ts1Rhr mice (*Mx2*, *Tmprss2*, *Ripk4*, *Prdm15*, *C2cd2* and *Zbtb21*). None of these six genes has been previously implicated in the etiology of CHD. However, a study of DS individuals found that congenital hearts defects were associated with two short copy number variants located between *RIPK4* and *PRDM15* and within *ZBTB21* respectively, implicating this region in DS-CHD (*35*). In addition, a recent study of rare copy number variants associated with AVSD in the non-DS population identified several patients with an extra copy of regions of Hsa21 ranging from 10-21 Mb and spanning both regions that we have identified in this mouse study, and proposed *DYRK1A* as a candidate gene for CHD (*36*).

Increased dosage of *Dyrk1a* is necessary but not sufficient to cause the mitochondrial defects and CHD, since these are not seen in Ts1Rhr mouse embryonic hearts despite 3 copies of *Dyrk1a*. It is unclear how elevated DYRK1A activity, acting with the unknown other causative gene(s), causes mitochondrial changes and CHD. One possibility is that increased DYRK1A inhibits the function of NFAT transcription factors, since DYRK1A phosphorylates NFAT proteins leading to their nuclear exclusion (*37*), and mouse embryos deficient in both NFATc3 and NFATc4 have impaired mitochondrial function and defective cardiac development (*38*). Indeed, DYRK1A in collaboration with RCAN1, another Hsa21-encoded gene, negatively regulates NFAT proteins and overexpression of both genes in the developing mouse leads to failure of outflow tract valve elongation (*37*). Although these are not the same defects as seen in DS, which are usually defects in septation, it supports the view that DYRK1A, acting through NFAT proteins can perturb cardiac development. Alternatively, DYRK1A may affect mitochondrial function through the SIRT1 protein deacetylase, since DYRK1A binds to, phosphorylates and activates SIRT1 and overexpression of SIRT1 in cardiomyocytes impairs their mitochondrial respiration (*39, 40*). SIRT1 in turn may be acting through PGC1α (PPARGC1A), a regulator of mitochondrial biogenesis (*41, 42*).

Increased *Dyrk1a* dosage is also necessary for the impaired proliferation, potentially by phosphorylating Cyclin D proteins leading to their degradation. This would result in reduced CDK4/6 activity, decreased phosphorylation of RB1, reduced activity of E2F transcription factors and less expression of E2F target genes which are required for G1 to S phase transition. Our study supports such a mechanism. In agreement with this, overexpression of DYRK1A in the cardiomyocytes of adult mice leads to reduced amounts of CCND2, RB1 phosphorylation and RB1/E2F signaling and hence to impaired proliferation (*20*). Conversely, inhibition of DYRK1A or cardiomyocyte-specific deletion of the *Dyrk1a* gene leads to increased cardiomyocyte proliferation and cardiac hypertrophy in adult mice (*43*). DYRK1A has been shown to phosphorylate LIN52, leading to assembly of the repressive form of the DREAM complex which promotes entry into quiescence, providing another mechanism by which DYRK1A overexpression may regulate proliferation (*44, 45*).

DYRK1A phosphorylates many proteins (*46, 47*). For example, in addition to the substrates described above (NFAT, SIRT1, CCND2 and LIN52), DYRK1A phosphorylates the C-terminal domain of RNA polymerase II, Alternative Splicing Factor (ASF) and CAS9, thereby regulating transcription, splicing and apoptosis (*48-51*). Further studies are needed to determine whether any of these DYRK1A targets is involved in DYRK1A-induced CHD.

It has been proposed that the increased expression of interferon response genes in DS is caused by a third copy of four interferon receptor genes located on Hsa21 (*52*). Since these expression changes are also seen in Dp3Tyb and Ts1Rhr mouse hearts which do not have an extra copy of the interferon receptor genes, our results show that one or more of the 31 genes present in three copies in Ts1Rhr mice can also cause these inflammatory gene expression changes. A recent report has shown that a third copy of the interferon receptor genes causes CHD in DS (*53*). However, since Dp3Tyb mice that do not have an increased dosage of these genes show CHD (*8*), and Dp1Tyb*Dyrk1a*$^{+/+/-}$ mice that still have three copies of the genes do not show CHD (this study), our results imply that increased dosage of the interferon receptor genes is neither necessary nor sufficient to cause CHD. Nonetheless it is possible that cardiac pathology results from a complex genetic interplay between *Dyrk1a*, the interferon receptor genes and other unknown causative genes.

This study has several limitations. It is unclear why Leucettinib-21 does not have a stronger effect on transcriptional changes in Dp1Tyb embryos, but possibilities include limited access of Leucettinib-21 to embryonic cardiac cells and pharmacokinetic issues such as a short half-life of the inhibitor in the embryo. Further work is needed to evaluate these issues. The work presented here shows that mitochondrial dysfunction and reduced cell proliferation correlate with congenital heart defects and that all three of these depend on a third copy of *Dyrk1a*, however the results do not prove that these cellular changes cause septation defects. Finally, the congenital heart defects are caused by increased dosage of at least two genes. In this study we have shown that one of these is *Dyrk1a*. Again, further work will be needed to identify the second causative gene.

We propose that CHD in DS arises in part from increased DYRK1A activity in cardiomyocytes leading to reduced proliferation and mitochondrial dysfunction (Fig. 8E). Furthermore, our systematic genetic mapping approach for dosage-sensitive genes can be used to identify causative genes and mechanisms responsible for the many other phenotypes of DS.

Materials and Methods

Study design

The aim of this study was to identify the genes that are necessary in three copies to cause congenital heart defects in DS, and to investigate how such increased dosage contributes to pathology. The study used the Dp1Tyb mouse model of DS in which embryos have heart defects similar to those seen in human DS. In addition, we also used tissue from human fetal hearts with DS, as well as euploid controls. Frozen human fetal hearts (13-14 pcw, 5 DS and 5 euploid age- and sex-matched samples) were obtained from the MRC-Wellcome Trust Human Developmental Biology Resource (HDBR) under appropriate ethical approval from the local Research Ethics Committees. UCL site REC reference: 18/LO/0822 – IRAS project ID: 244235 and Newcastle site REC reference: 18/NE/0290 – IRAS project ID: 250012. RNAseq was used to investigate transcriptional changes in human DS fetal hearts and in Dp1Tyb mouse embryonic hearts. Mitochondrial function and cell proliferation were measured in the mouse embryonic hearts. We used mouse genetics to identify one of the causative genes, *Dyrk1a*, and tested whether three copies of this gene were necessary to cause the transcriptional changes in Dp1Tyb embryonic hearts, as well as the changes in mitochondrial function and cell proliferation. Sample sizes were selected based on previous experience with similar methods. No randomization was performed. Investigators were blinded to genotype when scoring mouse embryonic hearts for the presence of heart defects. Human samples (DS and euploid) were balanced for age and sex. Mouse embryos were age-matched and mutant and control embryos were littermates. No samples were excluded from the study. Details on samples sizes representing biological replicates and statistical tests are detailed in figure legends and in the Statistical Analysis section of the Materials and Methods. Data are provided in Data file S1.

Mice

Mice carrying the following alleles have been described previously: Dp(16Lipi-Zbtb21)1TybEmcf (Dp1Tyb), Dp(16Mir802-Zbtb21)3TybEmcf (Dp3Tyb), Dp(16Cbr1-Fam3b)1Rhr (Ts1Rhr), *Kcnj6*$^{\text{tm1Stf}}$ (*Kcnj6*$^{-}$), *Dyrk1a*$^{\text{tm1Mla}}$ (*Dyrk1a*$^{-}$), and *Dyrk1a*$^{\text{tm2Yah}}$ (*Dyrk1a*$^{\text{K188R}}$) (*8, 25, 55-57*). Dp1Tyb mice have been deposited with JAX (strain #037183). Mice with the Del(16Mir802-Vps26c)4TybEmcf (Del4Tyb) allele were generated using an in vivo Cre-mediated recombination strategy by breeding female mice containing the *Hprt*$^{\text{tm1(cre)Mnn}}$ allele (*58*) and two loxP sites located in trans configuration on Mmu16 at the boundaries of the desired deletion, to C57BL/6J males. Cre activity in the female germline from the *Hprt*$^{\text{tm1(cre)Mnn}}$ allele resulted in occasional pups (5.3%) with recombination between the loxP sites generating the Del4Tyb deletion. Mice carrying the loxP sites were derived from targeting ES cells with MICER vectors MHPN219l02 (16:92850909 – 16:92859345 Mb, coordinates from mouse genome assembly GRCm39), located between *Runx1* and *Mir802,* and MHPP432c09 (16:94339475 – 16:94347709 Mb), located between *Vps26c* and *Dyrk1a* as previously described (*8*). The integrity of the Del4Tyb mutation was validated by comparative genome hybridization (fig. S4A). ES cells carrying the *Setd4*$^{\text{tm1a(KOMP)Wtsi}}$ allele (*59*) were obtained from the International Knockout Mouse Consortium and used to establish a mouse strain which was bred first to Tg(CAG-Flpo)1Afst mice (*60*) which express Flp in the germline to delete LacZ and Neo genes, generating mice with the *Setd4*$^{\text{tm1c(KOMP)Wtsi}}$ (*Setd4*$^{\text{fl}}$) allele in which exon 6 (ENSMUSE00001268769) is flanked by loxP sites. These in turn were bred to Tg(Prm-cre)70Og mice (*61*) expressing Cre in the male germline to generate mice bearing the *Setd4*$^{\text{tm1d(KOMP)Wtsi}}$ (*Setd4*$^{-}$) allele in which exon 6 had been deleted. Mice with the *Mir802*$^{\text{em1Tyb}}$ (*Mir802*$^{-}$) allele were generated by direct injection of Cas9 and 2 guide RNAs (5’-TCTACATAACCTACCGACTGCGG-3’ and 5’-ACGCCCTCCGAGGACACCCCAGG-

3') into mouse zygotes to generate a 141 bp deletion (16:93166602 - 16:93166742) of the *Mir802* gene. Since both Dp1Tyb and *Dyrk1a*$^{+/-}$ mice are poor breeders, we found it impossible to breed sufficient numbers of Dp1Tyb*Dyrk1a*$^{+/+/-}$ mice (nomenclature indicates mice with two WT alleles of *Dyrk1a* and one deleted allele) by simply intercrossing these strains. To overcome this, rare mice bearing both the Dp1Tyb and *Dyrk1a*$^{-}$ alleles were crossed to C57BL/6J mice and a pup was identified where a crossover had brought the two alleles onto the same chromosome. The resulting Dp1Tyb*Dyrk1a*$^{+/+/-}$ mice bred well and were maintained as a separate strain, with WT littermate embryos used as controls. RNAseq analysis confirmed that one *Dyrk1a* allele had a deletion of exons 7 and 8 (fig. S4B). All mice were bred and maintained on a C57BL/6J background (backcrossed for ≥ 10 generations), initially at the MRC National Institute for Medical Research and then at the Francis Crick Institute. All animal experiments were carried out under the authority of a Project Licence granted by the UK Home Office, and were approved by the Animal Welfare Ethical Review Body of the Francis Crick Institute. Numbers of protein-coding genes in different mouse strains were determined using the Biomart function in Ensembl on mouse genome assembly GRCm39, filtering for protein-coding genes, excluding three genes: ENSMUSG00000116933 which is a partial transcript for *Atp5o* (ENSMUSG00000022956), *Gm49711*, which is an alternatively spliced form of *Mrps6*, and *Gm49948* which is a fusion transcript of some exons from *Igsf5* and *Pcp4*. Note that the numbers of duplicated coding genes in the Dp strains have changed since our original publication (*8*), due to changes in gene annotation.

Statistical analysis

Statistical analysis of differential gene expression in RNAseq data was performed using the DESeq2 package. The significance threshold for the identification of differentially expressed genes, corrected for multiple testing, was set as an adjusted *P*-value <0.05.

Gene set enrichment analysis was carried out with the GSEA software, calculating a normalized enrichment score and a false discovery rate (FDR). An FDR <0.05 was considered significant. Statistical analysis of proteomic data was carried out using a Welch t-test to evaluate the significance of differences between samples of the two genotypes, generating an FDR corrected *P*-value; a *P*-value of <0.05 was considered significant. Other data were analyzed using Fisher's exact test, a two-sided Mann Whitney test or Kruskal-Wallis test as detailed in figure legends. A *P*-value of <0.05 was considered significant.

Supplementary Materials

Materials and Methods

Figures S1 – S6

Tables S1 – S10

Data file S1

References

1. S. E. Antonarakis, B. G. Skotko, M. S. Rafii, A. Strydom, S. E. Pape, D. W. Bianchi, S. L. Sherman, R. H. Reeves, Down syndrome. *Nat Rev Dis Primers* **6**, 9 (2020).
2. E. Lana-Elola, S. D. Watson-Scales, E. M. Fisher, V. L. Tybulewicz, Down syndrome: searching for the genetic culprits. *Dis. Model. Mech.* **4**, 586-95 (2011).
3. S. B. Freeman, L. H. Bean, E. G. Allen, S. W. Tinker, A. E. Locke, C. Druschel, C. A. Hobbs, P. A. Romitti, M. H. Royle, C. P. Torfs, K. J. Dooley, S. L. Sherman, Ethnicity, sex, and the incidence of congenital heart defects: a report from the National Down Syndrome Project. *Genet Med* **10**, 173-80 (2008).
4. S. L. Santoro, E. H. Steffensen, Congenital heart disease in Down syndrome – A review of temporal changes. *Journal of Congenital Cardiology* **5**, 1 (2021).
5. J. C. Vis, M. G. Duffels, M. M. Winter, M. E. Weijerman, J. M. Cobben, S. A. Huisman, B. J. Mulder, Down syndrome: a cardiovascular perspective. *J Intellect Disabil Res* **53**, 419-25 (2009).
6. D. R. Delany, S. S. Gaydos, D. A. Romeo, H. T. Henderson, K. L. Fogg, A. S. McKeta, M. N. Kavarana, J. M. Costello, Down syndrome and congenital heart disease: perioperative planning and management. *Journal of Congenital Cardiology* **5**, 7 (2021).
7. N. Mollo, R. Scognamiglio, A. Conti, S. Paladino, L. Nitsch, A. Izzo, Genetics and Molecular Basis of Congenital Heart Defects in Down Syndrome: Role of Extracellular Matrix Regulation. *Int J Mol Sci* **24**, (2023).
8. E. Lana-Elola, S. Watson-Scales, A. Slender, D. Gibbins, A. Martineau, C. Douglas, T. Mohun, E. M. Fisher, V. Tybulewicz, Genetic dissection of Down syndrome-associated congenital heart defects using a new mouse mapping panel. *Elife* **5**, 10.7554/eLife.11614 (2016).

9. E. Lana-Elola, H. Cater, S. Watson-Scales, S. Greenaway, J. Müller-Winkler, D. Gibbins, M. Nemes, A. Slender, T. Hough, P. Keskivali-Bond, C. L. Scudamore, E. M. Ross, G. T. Banks, H. Mobbs, T. Canonica, J. Tosh, S. Noy, M. Llorian, P. M. Nolan, J. L. Griffin, M. Good, M. Simon, A. M. Mallon, S. Wells, E. M. C. Fisher, V. L. J. Tybulewicz, Comprehensive phenotypic analysis of the Dp1Tyb mouse strain reveals a broad range of Down Syndrome-related phenotypes. *Dis. Model. Mech.* **14**, dmm049157 (2021).

10. A. Subramanian, P. Tamayo, V. K. Mootha, S. Mukherjee, B. L. Ebert, M. A. Gillette, A. Paulovich, S. L. Pomeroy, T. R. Golub, E. S. Lander, J. P. Mesirov, Gene set enrichment analysis: a knowledge-based approach for interpreting genome-wide expression profiles. *Proc Natl Acad Sci U S A* **102**, 15545-50 (2005).

11. Y. Xiao, M. C. Hill, M. Zhang, T. J. Martin, Y. Morikawa, S. Wang, A. R. Moise, J. D. Wythe, J. F. Martin, Hippo Signaling Plays an Essential Role in Cell State Transitions during Cardiac Fibroblast Development. *Dev Cell* **45**, 153-169 (2018).

12. M. Fischer, A. E. Schade, T. B. Branigan, G. A. Muller, J. A. DeCaprio, Coordinating gene expression during the cell cycle. *Trends Biochem Sci* **47**, 1009-1022 (2022).

13. J. R. Hom, R. A. Quintanilla, D. L. Hoffman, K. L. de Mesy Bentley, J. D. Molkentin, S. S. Sheu, G. A. Porter, Jr., The permeability transition pore controls cardiac mitochondrial maturation and myocyte differentiation. *Dev Cell* **21**, 469-78 (2011).

14. S. J. Kierans, C. T. Taylor, Regulation of glycolysis by the hypoxia-inducible factor (HIF): implications for cellular physiology. *J Physiol* **599**, 23-37 (2021).

15. K. Y. Aguilera, R. A. Brekken, Hypoxia Studies with Pimonidazole in vivo. *Bio Protoc* **4**, (2014).

16. C. Liu, M. Morishima, X. Jiang, T. Yu, K. Meng, D. Ray, A. Pao, P. Ye, M. S. Parmacek, Y. E. Yu, Engineered chromosome-based genetic mapping establishes

a 3.7 Mb critical genomic region for Down syndrome-associated heart defects in mice. *Hum Genet* **133**, 743-53 (2014).

17. W. J. Weninger, T. J. Mohun, Three-dimensional analysis of molecular signals with episcopic imaging techniques. *Methods Mol Biol* **411**, 35-46 (2007).
18. S. Najas, J. Arranz, P. A. Lochhead, A. L. Ashford, D. Oxley, J. M. Delabar, S. J. Cook, M. J. Barallobre, M. L. Arbones, DYRK1A-mediated Cyclin D1 Degradation in Neural Stem Cells Contributes to the Neurogenic Cortical Defects in Down Syndrome. *EBioMedicine* **2**, 120-34 (2015).
19. B. J. Thompson, R. Bhansali, L. Diebold, D. E. Cook, L. Stolzenburg, A. S. Casagrande, T. Besson, B. Leblond, L. Desire, S. Malinge, J. D. Crispino, DYRK1A controls the transition from proliferation to quiescence during lymphoid development by destabilizing Cyclin D3. *J Exp Med* **212**, 953-70 (2015).
20. S. Hille, F. Dierck, C. Kuhl, J. Sosna, S. Adam-Klages, D. Adam, R. Lullmann-Rauch, N. Frey, C. Kuhn, Dyrk1a regulates the cardiomyocyte cell cycle via D-cyclin-dependent Rb/E2f-signalling. *Cardiovasc Res* **110**, 381-94 (2016).
21. J. Y. Chen, J. R. Lin, F. C. Tsai, T. Meyer, Dosage of Dyrk1a shifts cells within a p21-cyclin D1 signaling map to control the decision to enter the cell cycle. *Mol Cell* **52**, 87-100 (2013).
22. U. Soppa, J. Schumacher, V. Florencio Ortiz, T. Pasqualon, F. J. Tejedor, W. Becker, The Down syndrome-related protein kinase DYRK1A phosphorylates p27(Kip1) and Cyclin D1 and induces cell cycle exit and neuronal differentiation. *Cell Cycle* **13**, 2084-100 (2014).
23. M. Alvarez, X. Altafaj, S. Aranda, S. de la Luna, DYRK1A autophosphorylation on serine residue 520 modulates its kinase activity via 14-3-3 binding. *Mol Biol Cell* **18**, 1167-78 (2007).

24. E. Deau, M. F. Lindberg, F. Miege, D. Roche, N. George, P. George, A. Kramer, S. Knapp, L. Meijer, Leucettinibs, a Class of DYRK/CLK Kinase Inhibitors Inspired by the Marine Sponge Natural Product Leucettamine B. *J Med Chem*, 10.1021/acs.jmedchem.3c00884 (2023).

25. V. Fotaki, M. Dierssen, S. Alcantara, S. Martinez, E. Marti, C. Casas, J. Visa, E. Soriano, X. Estivill, M. L. Arbones, Dyrk1A Haploinsufficiency Affects Viability and Causes Developmental Delay and Abnormal Brain Morphology in Mice. *Mol. Cell. Biol.* **22**, 6636-6647 (2002).

26. A. Conti, F. Fabbrini, P. D'Agostino, R. Negri, D. Greco, R. Genesio, M. D'Armiento, C. Olla, D. Paladini, M. Zannini, L. Nitsch, Altered expression of mitochondrial and extracellular matrix genes in the heart of human fetuses with chromosome 21 trisomy. *BMC Genomics* **8**, 268 (2007).

27. Y. Liu, C. Borel, L. Li, T. Muller, E. G. Williams, P. L. Germain, M. Buljan, T. Sajic, P. J. Boersema, W. Shao, M. Faini, G. Testa, A. Beyer, S. E. Antonarakis, R. Aebersold, Systematic proteome and proteostasis profiling in human Trisomy 21 fibroblast cells. *Nat Commun* **8**, 1212 (2017).

28. A. Izzo, N. Mollo, M. Nitti, S. Paladino, G. Cali, R. Genesio, F. Bonfiglio, R. Cicatiello, M. Barbato, V. Sarnataro, A. Conti, L. Nitsch, Mitochondrial dysfunction in down syndrome: molecular mechanisms and therapeutic targets. *Mol Med* **24**, 2 (2018).

29. D. Valenti, N. Braidy, D. De Rasmo, A. Signorile, L. Rossi, A. G. Atanasov, M. Volpicella, A. Henrion-Caude, S. M. Nabavi, R. A. Vacca, Mitochondria as pharmacological targets in Down syndrome. *Free Radic Biol Med* **114**, 69-83 (2018).

30. M. P. Bayona-Bafaluy, N. Garrido-Perez, P. Meade, E. Iglesias, I. Jimenez-Salvador, J. Montoya, C. Martinez-Cue, E. Ruiz-Pesini, Down syndrome is an oxidative phosphorylation disorder. *Redox Biol* **41**, 101871 (2021).
31. J. Busciglio, A. Pelsman, C. Wong, G. Pigino, M. Yuan, H. Mori, B. A. Yankner, Altered metabolism of the amyloid beta precursor protein is associated with mitochondrial dysfunction in Down's syndrome. *Neuron* **33**, 677-88 (2002).
32. P. Helguera, J. Seiglie, J. Rodriguez, M. Hanna, G. Helguera, J. Busciglio, Adaptive downregulation of mitochondrial function in down syndrome. *Cell Metab* **17**, 132-40 (2013).
33. C. Piccoli, A. Izzo, R. Scrima, F. Bonfiglio, R. Manco, R. Negri, G. Quarato, O. Cela, M. Ripoli, M. Prisco, F. Gentile, G. Cali, P. Pinton, A. Conti, L. Nitsch, N. Capitanio, Chronic pro-oxidative state and mitochondrial dysfunctions are more pronounced in fibroblasts from Down syndrome foeti with congenital heart defects. *Hum Mol Genet* **22**, 1218-32 (2013).
34. A. Izzo, M. Nitti, N. Mollo, S. Paladino, C. Procaccini, D. Faicchia, G. Cali, R. Genesio, F. Bonfiglio, R. Cicatiello, E. Polishchuk, R. Polishchuk, P. Pinton, G. Matarese, A. Conti, L. Nitsch, Metformin restores the mitochondrial network and reverses mitochondrial dysfunction in Down syndrome cells. *Hum Mol Genet* **26**, 1056-1069 (2017).
35. M. R. Sailani, P. Makrythanasis, A. Valsesia, F. A. Santoni, S. Deutsch, K. Popadin, C. Borel, E. Migliavacca, A. J. Sharp, G. Duriaux Sail, E. Falconnet, K. Rabionet, C. Serra-Juhe, S. Vicari, D. Laux, Y. Grattau, G. Dembour, A. Megarbane, R. Touraine, S. Stora, S. Kitsiou, H. Fryssira, C. Chatzisevastou-Loukidou, E. Kanavakis, G. Merla, D. Bonnet, L. A. Perez-Jurado, X. Estivill, J. M. Delabar, S. E. Antonarakis, The complex SNP and CNV genetic architecture of the increased

risk of congenital heart defects in Down syndrome. *Genome Res* **23**, 1410-21 (2013).

36. H. Hu, Z. Geng, S. Zhang, Y. Xu, Q. Wang, S. Chen, B. Zhang, K. Sun, Y. Lu, Rare copy number variation analysis identifies disease-related variants in atrioventricular septal defect patients. *Front Genet* **14**, 1075349 (2023).
37. J. R. Arron, M. M. Winslow, A. Polleri, C. P. Chang, H. Wu, X. Gao, J. R. Neilson, L. Chen, J. J. Heit, S. K. Kim, N. Yamasaki, T. Miyakawa, U. Francke, I. A. Graef, G. R. Crabtree, NFAT dysregulation by increased dosage of DSCR1 and DYRK1A on chromosome 21. *Nature* **441**, 595-600 (2006).
38. P. B. Bushdid, H. Osinska, R. R. Waclaw, J. D. Molkentin, K. E. Yutzey, NFATc3 and NFATc4 are required for cardiac development and mitochondrial function. *Circ Res* **92**, 1305-13 (2003).
39. X. Guo, J. G. Williams, T. T. Schug, X. Li, DYRK1A and DYRK3 promote cell survival through phosphorylation and activation of SIRT1. *J Biol Chem* **285**, 13223-32 (2010).
40. T. Kawashima, Y. Inuzuka, J. Okuda, T. Kato, S. Niizuma, Y. Tamaki, Y. Iwanaga, A. Kawamoto, M. Narazaki, T. Matsuda, S. Adachi, G. Takemura, T. Kita, T. Kimura, T. Shioi, Constitutive SIRT1 overexpression impairs mitochondria and reduces cardiac function in mice. *J Mol Cell Cardiol* **51**, 1026-36 (2011).
41. J. T. Rodgers, C. Lerin, W. Haas, S. P. Gygi, B. M. Spiegelman, P. Puigserver, Nutrient control of glucose homeostasis through a complex of PGC-1alpha and SIRT1. *Nature* **434**, 113-8 (2005).
42. C. Canto, J. Auwerx, PGC-1alpha, SIRT1 and AMPK, an energy sensing network that controls energy expenditure. *Curr Opin Lipidol* **20**, 98-105 (2009).

43. A. Young, L. A. Bradley, E. Farrar, H. O. Bilcheck, S. Tkachenko, J. J. Saucerman, S. Bekiranov, M. J. Wolf, Inhibition of DYRK1a Enhances Cardiomyocyte Cycling After Myocardial Infarction. *Circ Res* **130**, 1345-1361 (2022).

44. L. Litovchick, L. A. Florens, S. K. Swanson, M. P. Washburn, J. A. DeCaprio, DYRK1A protein kinase promotes quiescence and senescence through DREAM complex assembly. *Genes Dev* **25**, 801-13 (2011).

45. P. Wang, E. Karakose, C. Argmann, H. Wang, M. Balev, R. I. Brody, H. G. Rivas, X. Liu, O. Wood, H. Liu, L. Choleva, D. Hasson, E. Bernstein, J. A. Paulo, D. K. Scott, L. Lambertini, J. A. DeCaprio, A. F. Stewart, Disrupting the DREAM complex enables proliferation of adult human pancreatic beta cells. *J Clin Invest* **132**, e157086 (2022).

46. M. F. Lindberg, L. Meijer, Dual-Specificity, Tyrosine Phosphorylation-Regulated Kinases (DYRKs) and cdc2-Like Kinases (CLKs) in Human Disease, an Overview. *Int J Mol Sci* **22**, (2021).

47. L. J. Kay, T. K. Smulders-Srinivasan, M. Soundararajan, Understanding the Multifaceted Role of Human Down Syndrome Kinase DYRK1A. *Adv Protein Chem Struct Biol* **105**, 127-71 (2016).

48. C. Di Vona, D. Bezdan, A. B. Islam, E. Salichs, N. Lopez-Bigas, S. Ossowski, S. de la Luna, Chromatin-wide profiling of DYRK1A reveals a role as a gene-specific RNA polymerase II CTD kinase. *Mol Cell* **57**, 506-20 (2015).

49. J. Shi, T. Zhang, C. Zhou, M. O. Chohan, X. Gu, J. Wegiel, J. Zhou, Y. W. Hwang, K. Iqbal, I. Grundke-Iqbal, C. X. Gong, F. Liu, Increased dosage of Dyrk1A alters alternative splicing factor (ASF)-regulated alternative splicing of tau in Down syndrome. *J Biol Chem* **283**, 28660-9 (2008).

50. A. Seifert, L. A. Allan, P. R. Clarke, DYRK1A phosphorylates caspase 9 at an inhibitory site and is potently inhibited in human cells by harmine. *FEBS J* **275**, 6268-80 (2008).

51. A. Laguna, S. Aranda, M. J. Barallobre, R. Barhoum, E. Fernandez, V. Fotaki, J. M. Delabar, S. de la Luna, P. de la Villa, M. L. Arbones, The protein kinase DYRK1A regulates caspase-9-mediated apoptosis during retina development. *Dev Cell* **15**, 841-53 (2008).

52. K. D. Sullivan, H. C. Lewis, A. A. Hill, A. Pandey, L. P. Jackson, J. M. Cabral, K. P. Smith, L. A. Liggett, E. B. Gomez, M. D. Galbraith, J. DeGregori, J. M. Espinosa, Trisomy 21 consistently activates the interferon response. *Elife* **5**, (2016).

53. K. A. Waugh, R. Minter, J. Baxter, C. Chi, M. D. Galbraith, K. D. Tuttle, N. P. Eduthan, K. T. Kinning, Z. Andrysik, P. Araya, H. Dougherty, L. N. Dunn, M. Ludwig, K. A. Schade, D. Tracy, K. P. Smith, R. E. Granrath, N. Busquet, S. Khanal, R. D. Anderson, L. L. Cox, B. E. Estrada, A. L. Rachubinski, H. R. Lyford, E. C. Britton, K. A. Fantauzzo, D. J. Orlicky, J. L. Matsuda, K. Song, T. C. Cox, K. D. Sullivan, J. M. Espinosa, Triplication of the interferon receptor locus contributes to hallmarks of Down syndrome in a mouse model. *Nat Genet* **55**, 1034-1047 (2023).

54. A. Chaudhry, R. Shi, D. S. Luciani, A pipeline for multidimensional confocal analysis of mitochondrial morphology, function, and dynamics in pancreatic beta-cells. *Am J Physiol Endocrinol Metab* **318**, E87-E101 (2020).

55. L. E. Olson, J. T. Richtsmeier, J. Leszl, R. H. Reeves, A Chromosome 21 Critical Region Does Not Cause Specific Down Syndrome Phenotypes. *Science* **306**, 687-690 (2004).

56. S. Signorini, Y. J. Liao, S. A. Duncan, L. Y. Jan, M. Stoffel, Normal cerebellar development but susceptibility to seizures in mice lacking G protein-coupled, inwardly rectifying K+ channel GIRK2. *Proc Natl Acad Sci U S A* **94**, 923-7 (1997).

57. M. V. Hinckelmann, A. Dubos, V. Artot, G. Rudolf, T. L. Nguyen, P. Tilly, V. Nalesso, M. d. M. Muniz Moreno, M.-C. Birling, J. Godin, V. Brault, Y. Herault, Interneuron migration defects during corticogenesis contribute to Dyrk1a haploinsufficiency syndrome pathogenesis via actomyosin dynamics deregulations. *bioRxiv*, 2023.11.09.566424 (2023).

58. S. H. Tang, F. J. Silva, W. M. Tsark, J. R. Mann, A Cre/loxP-deleter transgenic line in mouse strain 129S1/SvImJ. *Genesis* **32**, 199-202 (2002).

59. W. C. Skarnes, B. Rosen, A. P. West, M. Koutsourakis, W. Bushell, V. Iyer, A. O. Mujica, M. Thomas, J. Harrow, T. Cox, D. Jackson, J. Severin, P. Biggs, J. Fu, M. Nefedov, P. J. de Jong, A. F. Stewart, A. Bradley, A conditional knockout resource for the genome-wide study of mouse gene function. *Nature* **474**, 337-42 (2011).

60. A. Kranz, J. Fu, K. Duerschke, S. Weidlich, R. Naumann, A. F. Stewart, K. Anastassiadis, An improved Flp deleter mouse in C57Bl/6 based on Flpo recombinase. *Genesis* **48**, 512-20 (2010).

61. S. O'Gorman, N. A. Dagenais, M. Qian, Y. Marchuk, Protamine-Cre recombinase transgenes efficiently recombine target sequences in the male germ line of mice, but not in embryonic stem cells. *Proc. Natl. Acad. Sci. USA* **94**, 14602-7 (1997).

62. A. M. Bolger, M. Lohse, B. Usadel, Trimmomatic: a flexible trimmer for Illumina sequence data. *Bioinformatics* **30**, 2114-20 (2014).

63. B. Li, C. N. Dewey, RSEM: accurate transcript quantification from RNA-Seq data with or without a reference genome. *BMC Bioinformatics* **12**, 323 (2011).

64. A. Dobin, C. A. Davis, F. Schlesinger, J. Drenkow, C. Zaleski, S. Jha, P. Batut, M. Chaisson, T. R. Gingeras, STAR: ultrafast universal RNA-seq aligner. *Bioinformatics* **29**, 15-21 (2013).

65. G. Warnes, B. Bolker, L. Bonebakker, R. Gentleman, W. Huber, A. Liaw, T. Lumley, M. Mächler, A. Magnusson, S. Möller, M. A. Schwartz, B. Venables, *gplots: Various R programming tools for plotting data*. (2015), vol. 2.

66. M. I. Love, W. Huber, S. Anders, Moderated estimation of fold change and dispersion for RNA-seq data with DESeq2. *Genome Biol.* **15**, 550 (2014).

67. R_CoreTeam, R: A language and environment for statistical computing. R Foundation for Statistical Computing. https://www.R-project.org/ (2021).

68. P. Di Tommaso, M. Chatzou, E. W. Floden, P. P. Barja, E. Palumbo, C. Notredame, Nextflow enables reproducible computational workflows. *Nat Biotechnol* **35**, 316-319 (2017).

69. P. A. Ewels, A. Peltzer, S. Fillinger, H. Patel, J. Alneberg, A. Wilm, M. U. Garcia, P. Di Tommaso, S. Nahnsen, The nf-core framework for community-curated bioinformatics pipelines. *Nat Biotechnol* **38**, 276-278 (2020).

70. N. Ignatiadis, B. Klaus, J. B. Zaugg, W. Huber, Data-driven hypothesis weighting increases detection power in genome-scale multiple testing. *Nat Methods* **13**, 577-80 (2016).

71. N. Ignatiadis, W. Huber, Covariate powered cross-weighted multiple testing. *arXiv*, doi:arXiv:1701.05179 (2017).

72. A. Butler, P. Hoffman, P. Smibert, E. Papalexi, R. Satija, Integrating single-cell transcriptomic data across different conditions, technologies, and species. *Nat Biotechnol* **36**, 411-420 (2018).

73. Y. Perez-Riverol, A. Csordas, J. Bai, M. Bernal-Llinares, S. Hewapathirana, D. J. Kundu, A. Inuganti, J. Griss, G. Mayer, M. Eisenacher, E. Perez, J. Uszkoreit, J. Pfeuffer, T. Sachsenberg, S. Yilmaz, S. Tiwary, J. Cox, E. Audain, M. Walzer, A. F. Jarnuczak, T. Ternent, A. Brazma, J. A. Vizcaino, The PRIDE database and

related tools and resources in 2019: improving support for quantification data. *Nucleic Acids Res* **47**, D442-D450 (2019).

74. W. J. Weninger, S. H. Geyer, T. J. Mohun, D. Rasskin-Gutman, T. Matsui, I. Ribeiro, F. Costa Lda, J. C. Izpisua-Belmonte, G. B. Muller, High-resolution episcopic microscopy: a rapid technique for high detailed 3D analysis of gene activity in the context of tissue architecture and morphology. *Anat Embryol (Berl)* **211**, 213-21 (2006).

75. A. Rosset, L. Spadola, O. Ratib, OsiriX: an open-source software for navigating in multidimensional DICOM images. *J Digit Imaging* **17**, 205-16 (2004).

76. L. Dunlevy, M. Bennett, A. Slender, E. Lana-Elola, V. L. Tybulewicz, E. M. Fisher, T. Mohun, Down's syndrome-like cardiac developmental defects in embryos of the transchromosomic Tc1 mouse. *Cardiovasc Res* **88**, 287-95 (2010).

77. A. Ponten, S. Walsh, D. Malan, X. Xian, S. Scheele, L. Tarnawski, B. K. Fleischmann, S. Jovinge, FACS-based isolation, propagation and characterization of mouse embryonic cardiomyocytes based on VCAM-1 surface marker expression. *PLoS One* **8**, e82403 (2013).

Acknowledgments:

We thank Dr. J. Turner for critical reading of this manuscript. We thank Dr. F. Prin for help with HREM and Dr. M. Howell for help with high throughput analysis of mitochondrial morphology. We thank the Advanced Sequencing, Proteomics, High Throughput Screening, Flow Cytometry, Advanced Light Microscopy, Experimental Histopathology, Genetic Manipulation and Biological Research Facilities of the Francis Crick Institute for sequencing, proteomics, mitochondrial morphology analysis, flow cytometry, imaging, histology, generation of genetically altered mice and for animal husbandry. We thank Dr. M. Arbones and Dr. C. Lüscher for mouse strains.

Funding

This work was supported by the Wellcome Trust (grants 098327 and 098328 to VLJT and EMCF) and by the Francis Crick Institute (CC2080 to VLJT and CC2081 to MGG) which receives its core funding from Cancer Research UK (CC2080, CC2081), the UK Medical Research Council (CC2080, CC2081), and the Wellcome Trust (CC2080, CC2081). The human embryonic and fetal material was provided by the Human Developmental Biology Resource (https://www.hdbr.org/) supported by a joint MRC/Wellcome Trust grant (MR/R006237/1). This research was funded in whole, or in part, by the Wellcome Trust. For the purpose of Open Access, the authors have applied a CC-BY public copyright licence to any Author Accepted Manuscript version arising from this submission.

Author Contributions

VLJT and EMCF design the study and obtained funding. VLJT administered the project. EL-E, RA, CaB, DG, MHH, and DH performed the HREM experiments. EL-E, ML, TG and HF conducted and analyzed the transcriptome, proteome, and phospho-proteome experiments. RA and ClB performed and analyzed the metabolic analysis experiments. RA and O-RS performed and analyzed the mitochondrial shape experiments. EL-E and RA performed and analyzed the immunoblot experiments. EL-E performed and analyzed the RNAscope experiment. RA performed and analyzed the Hypoxyprobe and flow cytometry experiments. EL-E and RA conducted and analyzed the Leucettinib-21 treatment experiment. EL-E and SW-S generated the Dp1Tyb, Dp3Tyb, Del4Tyb and *Mir802*$^{\mathrm{em1Tyb}}$ mice. VB and YH generated the *Dyrk1a*$^{\mathrm{tm2Yah}}$ (*Dyrk1a*$^{\mathrm{K188R}}$) mice. DG, MHH, CaB and DH managed mouse colonies. ED and LM generated the Leucettinib-21 and iso-Leucettinib-21 compounds. APS, MG, EMCF and VLJT supervised the work. EL-E, RA and ML visualized the data. EL-E, RA, EMCF and VLJT wrote and edited the manuscript. All authors reviewed and approved the manuscript.

Competing interests

L.M. is a founder of Perha Pharmaceuticals. L.M. and E.M. are co-inventors in the Leucettinibs patents (New imidazolone derivatives as inhibitors of protein kinases, in particular DYRK1A, CLK1 and/or CLK4; EP4143185, PCT/EP2021/061349, WO2021219828A1, EP4173675A1, EP4173673, EP4173674). All other authors have no competing interests.

Data and materials availability

All data associated with this study are present in the paper or supplementary materials. Dp1Tyb mice are available from JAX (strain #037183). Dp1Tyb and Dp3Tyb mice are available from the European Mouse Mutant Archive. Mice carrying the Del4Tyb, *Setd4*$^{tm1d(KOMP)Wtsi}$ and *Mir802*^{em1Tyb} alleles are available on request to the corresponding author under an MTA. All bulk and single-cell RNAseq data have been deposited in the Gene Expression Omnibus, accession code: GSE196447. Mass spectrometry proteomic data have been deposited in the ProteomeXchange through the PRIDE partner repository, dataset identifier: PXD013053.

Figure Legends

Figure 1. Transcriptomic similarities in embryonic hearts from human fetuses with DS and mouse models of DS. (**A, B**) RNAseq analysis of human DS and euploid embryonic hearts (13-14 post-conception weeks, *n*=5), showing (A) a volcano plot of fold-change in gene expression (DS versus euploid) against adjusted *P*-value for significance of the difference, showing Hsa21 genes (red), differentially expressed genes (blue), and *DYRK1A* (black) (B) unsupervised hierarchical clustering of the 10 samples showing heatmap of differentially expressed genes (**C, D**) RNAseq analysis of E13.5 hearts from WT and Dp1Tyb embryos (*n*=5) showing (C) a volcano plot as in A, indicating genes in 3 copies in Dp1Tyb mice (red), differentially expressed genes (blue), and *Dyrk1a* (black) and (D) hierarchical clustering of the samples as in B. (**E**) Hallmark gene sets from the Molecular Signatures Database that are significantly enriched or depleted (GSEA, ≤5% FDR) in both human DS and Dp1Tyb mouse hearts; NES, normalized enrichment scores. Gene sets showing the same direction of change in human and mouse data are indicated in bold. (**F**) Map of Hsa21 (length in Mb) showing cytogenetic bands and regions of orthology to Mmu10, Mmu17 and Mmu16 (grey) and indicating regions of Mmu16 that are duplicated in mouse strains (bold) that show CHD (yellow) and that do not (black); numbers of coding genes indicated below duplicated regions. (**G**) Comparison of dysregulated gene sets determined by GSEA of RNAseq data from human DS versus euploid embryonic hearts and in hearts from Dp1Tyb, Dp3Tyb and Ts1Rhr mouse embryos compared to WT controls. All show heart defects except Ts1Rhr mice. Colors and sizes of circles indicate NES and FDR q-value, respectively.

Figure 2. scRNAseq reveals similar gene expression changes across different cell types in Dp1Tyb mouse embryonic hearts. (**A**) Uniform Manifold Approximation and

Projection (UMAP) clustering of scRNAseq data pooled from WT, Dp1Tyb and Dp1Tyb*Dyrk1a*$^{+/+/-}$ E13.5 mouse hearts. Each dot represents a single cell; colors indicate 14 clusters whose identity was inferred based on expression of markers genes. V, ventricular; CM, cardiomyocytes; AVC, atrioventricular canal; OFT, outflow tract. (**B**) Violin plots showing the expression of representative marker genes across the 14 clusters; Y-axis shows the log-scale normalized read count. (**C**) Stacked column plot showing the percentage of cells in each of the 14 cell populations, colored according to cluster designation. Clusters with significantly altered percentages in Dp1Tyb hearts compared to WT are indicated; Fisher's exact test, * $0.01 < P < 0.05$, ** $0.001 < P < 0.01$, *** $P < 0.001$. (**D**) GSEA of Dp1Tyb versus WT (a) or Dp1Tyb versus Dp1Tyb*Dyrk1a*$^{+/+/-}$ (b) scRNAseq data from the 11 most abundant clusters analyzed individually and pooled (pseudo-bulk), showing key pathways and their NES. Colors and sizes of circles indicate NES and FDR q-value, respectively. Sample numbers: *n*=2 WT, 1 Dp1Tyb, 2 Dp1Tyb*Dyrk1a*$^{+/+/-}$ embryonic hearts.

Figure 3. **Proliferative defects in Dp1Tyb embryonic hearts.**

(**A**) Flow cytometric analysis of freshly isolated embryonic mouse hearts pulsed with EdU. EdU and DNA content of cardiomyocytes (CD106^{+}CD31^{-}) and endocardial cells (CD106^{-} CD31^{+}) were used to distinguish cells in G1, S and G2/M phases. Numbers indicate percentage of cells in gates. (**B**) Mean (±SEM) percentage of cells in each cell cycle phase taken from data as in A. *n*=38 WT, 14 Dp1Tyb, 12 Dp1TybDyrk1a$^{+/+/-}$ embryonic mouse hearts. (**C**) Diagram showing how DYRK1A may regulate the cell cycle. Cyclin D2 (CCND2) in complex with CDK4/6 phosphorylates RB1 promoting cell cycle progression. DYRK1A phosphorylates CCND2 leading to its degradation thereby causing reduced CDK4/6 activity, reduced RB1 phosphorylation and impaired cell cycle progression. (**D**) Representative immunoblot analysis of lysates from WT, Dp1Tyb and Dp1Tyb*Dyrk1a*$^{+/+/-}$

E13.5 embryonic hearts probed with antibodies to phospho-RB1 (p-RB1) and GAPDH. Each lane represents an individual embryonic heart. (**E**) Mean p-RB1 abundance determined by immunoblots such as those in D, normalized to GAPDH and to the mean of WT samples which was set to 1. Dots represent individual embryos. *n*=27 WT, 14 Dp1Tyb, 12 Dp1TybDyrk1a$^{+/+/-}$ embryonic hearts. Statistical significance was calculated using a Kruskal-Wallis test; * $0.01 < P < 0.05$, ** $0.001 < P < 0.01$; ns, not significant.

Figure 4. **Mitochondrial defects in Dp1Tyb mouse embryonic cardiomyocytes.**

(**A**) Flow cytometric analysis showing gating strategy used to measure mitochondrial mass (MTG) and mitochondrial potential (TMRM) in cardiomyocytes (CD106$^+$CD31$^-$) and endocardial cells (CD106$^-$CD31$^+$) from E13.5 mouse embryonic hearts of the indicated genotypes. Cardiomyocytes were subdivided into cells that have a high (TMRM-H) and medium (TMRM-M) potential. Numbers indicate percentage of cells in gates. (**B**) Mean fluorescence intensity (MFI) of MTG and TMRM in endocardial cells and of MTG in cardiomyocytes normalized to the average of WT samples which was set to 1. For cardiomyocytes mitochondrial potential was measured using a TMRM-H/TMRM-M ratio. Dots represent individual embryos. *n*=17 WT, 13 Dp1Tyb, 15 Dp1TybDyrk1a$^{+/+/-}$ embryonic hearts. (**C**) Representative confocal microscopy images of cells from E13.5 mouse hearts of the indicated genotypes showing staining with MitoTracker Deep Red (MTDR – mitochondria, red), anti-CD106 (cardiomyocytes, green) and DAPI (blue). Images show a maximum projection of Z-stacks from 0 to 3 µm with a step size of 1 µm. Insets are enlarged images of the region in the dashed square showing the mitochondrial network. Scale bar 50 µm. (**D**) Violin plots of mitochondrial aspect ratio and form factor in cardiomyocytes (CD106$^+$) determined from images such as those in C (fig. S3A, B). Aspect ratio and form factor are measures of distortion from circularity and degree of branching, respectively (*54*). Black lines indicate median, dotted lines indicate 25th and

75th centiles. *n*=25 WT, 10 Dp1Tyb, 17 Dp1TybDyrk1a$^{+/+/-}$ mouse embryonic hearts. (**E**) Mean±SEM oxygen consumption rate (OCR) in E13.5 mouse heart cells from embryos of the indicated genotypes analyzed using a Seahorse analyzer with oligomycin (ATP synthase inhibitor), FCCP (depolarizes mitochondrial membrane potential), and rotenone and antimycin (complex I and III inhibitors) added at the indicated times. Basal respiration rate was calculated from the mean of the first three measurements, maximal respiration rate from the three time points after addition of FCCP. (**F**) Mean basal and maximal respiration rates of E13.5 mouse heart cells normalized to the mean rates in WT hearts. Dots represent individual embryos. *n*=14 WT, 6 Dp1Tyb, 8 Dp1Tyb*Dyrk1a*$^{+/+/-}$ embryonic hearts. (**G**) Mean±SEM extracellular acidification rate (ECAR) in E13.5 mouse heart cells from embryos of the indicated genotypes analyzed using a Seahorse analyzer with glucose, oligomycin (ATP synthase inhibitor) and 2 deoxy-glucose (2-DG, competitive inhibitor of glucose) added at the indicated times. Glycolysis rate was calculated as the difference between the mean ECAR of the three measurements before and after glucose injection. (**H**) Mean glycolysis rates of E13.5 mouse heart cells normalized to the mean rates in WT hearts. Dots represent individual embryos. *n*=35 WT, 8 Dp1Tyb, 10 Dp1TybDyrk1a$^{+/+/-}$ embryonic hearts. (**I**) Representative images of sections of E13.5 mouse hearts of the indicated genotypes showing a 4-chamber view stained with anti-Endomucin (endothelial cells, green), anti-Hypoxyprobe (hypoxia, red) and DAPI (blue). Dashed line indicates a region of interest (ROI) encompassing the ventricles and the atrioventricular cushions. Scale bar 200 μm. (**J**) MFI of anti-Hypoxyprobe in ROI determined from images such as those in I. *n*=4 WT, 6 Dp1Tyb mouse embryonic hearts. Dots represent individual embryos. LV, left ventricle; RV, right ventricle; LA, left atrium; RA, right atrium; AVC, atrioventricular cushion; VS, ventricular septum. Statistical significance was calculated using a Kruskal-Wallis (B, D, F, H) or Mann Whitney test (J), * $0.01 < P < 0.05$, ** $0.001 < P < 0.01$, **** $P < 0.0001$; ns, not significant.

Figure 5. Three copies of *Dyrk1a* are necessary to cause heart defects.

(**A**) Map of Hsa21 showing regions of orthology to Mmu10, Mmu17 and Mmu16 (grey) and indicating regions of Mmu16 that are duplicated in mouse strains that show CHD (yellow) and in those that do not (black); genes at boundaries of these duplications are indicated next to the Mmu16 map; numbers of coding genes indicated below duplicated regions. Two genetic intervals containing 3 and 2 candidate genes for CHD are indicated in orange and blue, respectively. (**B-G**) Graphs of percentage of CHD in E14.5 mouse embryonic hearts from the indicated mouse models, indicating the frequency of AVSD and other CHD, which are predominantly VSDs and occasionally outflow tract defects such as overriding aorta. The orange and blue boxes highlight the genes found in the 2 candidate regions. The cross of Dp1Tyb to Del4Tyb was used to determine if 3 copies of *Cbr1* are required for heart defects. Numbers of embryonic hearts analyzed: (B) WT (*n*=25), Dp1Tyb (*n*=20), Dp1Tyb*Mir802*$^{+/+/-}$ (*n*=27) hearts with two copies of *Mir802*; (C) WT (*n*=24), Dp1Tyb (*n*=23), Dp1Tyb*Setd4*$^{+/+/-}$ (*n*=26) hearts with two copies of *Setd4*; (D) WT (*n*=7), Dp1Tyb (*n*=13), Dp1TybDel4Tyb (*n*=15) hearts with two copies of the region deleted in Del4Tyb; (E) WT (*n*=34), Dp1Tyb (*n*=41), Dp1Tyb*Kcnj6*$^{+/+/-}$ (*n*=30) hearts with two copies of *Kcnj6*; (F) WT (*n*=91), Dp1Tyb (*n*=86), Dp1Tyb*Dyrk1a*$^{+/+/-}$ (*n*=23) hearts with two copies of *Dyrk1a*; (G) WT (*n*=30), Dp1Tyb (*n*=23), Dp1Tyb*Dyrk1a*$^{+/+/K188R}$ (*n*=44) hearts with two WT and one kinase-inactive allele of *Dyrk1a*. Fisher's exact test, * $0.01 < P < 0.05$, ** $0.001 < P < 0.01$, *** $P < 0.001$ for difference in number of total CHD, except for Dp1Tyb*Dyrk1a*$^{+/+/K188R}$ cohort, where statistics were calculated for number of AVSD; ns, not significant. (**H**) 3 Dimensional high resolution episcopic microscopy (HREM) rendering of WT, Dp1Tyb, Dp1Tyb*Dyrk1a*$^{+/+/-}$ and Dp1Tyb*Dyrk1a*$^{+/+/K188R}$ mouse hearts, eroded to show an anterior four-chamber view (top and middle) and a two-chamber view (bottom) seen from the atria at the level of the atrioventricular canal. Top and bottom rows show eroded 3D views, middle row shows 2D sections at the same level as shown in the top row. Red arrowheads indicate VSD (top, middle) or AVSD (bottom). iAVC, inferior atrio-ventricular cushion; LV, left ventricle; MV, mitral valve; RV, right ventricle; sAVC, superior atrio-ventricular cushion; TV, tricuspid valve; VS, ventricular septum.

Figure 6. Increased dosage of *Dyrk1a* causes key transcriptional changes in Dp1Tyb mouse embryonic hearts.

(**A**) Volcano plots showing fold-change in gene expression in E13.5 mouse embryonic hearts, Dp1Tyb*Dyrk1a*$^{+/+/-}$ versus WT (left) and Dp1Tyb versus Dp1Tyb*Dyrk1a*$^{+/+/-}$ (right), plotted against adjusted *P*-value for significance of the difference. Genes present in three copies in Dp1Tyb mice (red) and differentially expressed genes (blue) and *Dyrk1a* (black) are indicated. (**B**) Volcano plots showing fold-change in abundance of proteins and phosphorylated sites in Dp1Tyb versus Dp1Tyb*Dyrk1a*$^{+/+/-}$ E13.5 hearts. DYRK1A, CCND1, CCND2 and CCND3 are indicated in green on the proteome plot (left); phosphorylated sites known to be DYRK1A targets and an autophosphorylation site on DYRK1A are indicated in green on the phosphoproteome plot (right). (**C**) Comparison of dysregulated pathways determined by GSEA of RNAseq and proteomic experiments. Colors and sizes of circles indicate NES and FDR q-value, respectively. Sample numbers: *n*=5 embryonic hearts.

Figure 7. *Dyrk1a* expression in a broad range of cell types in the developing mouse heart.

(**A**) Violin plots showing expression of *Dyrk1a* in mouse E13.5 hearts across 14 cell clusters identified in Fig. 2B. Dots indicate single cells. Sample numbers: *n*=5 embryonic hearts. (**B**) Left, schematic illustrations of a sagittal section (top) of an E12.5 mouse heart and a 4-chamber view (bottom) of an E14.5 heart. Right, RNAscope analysis of *Dyrk1a* expression (brown dots) in sections of the right ventricle myocardial wall (1) and atrioventricular cushions (2) at E12.5 and right ventricular myocardial wall (3) and ventricular septum (4) at E14.5; sections were counterstained with hematoxylin (blue). Scale bar 50 µm. iAVC, inferior atrioventricular cushion; LA, left atrium; LV, left ventricle; OFT, outflow tract; PT, pulmonary trunk; RA, right atrium; RV, right ventricle; sAVC, superior atrioventricular cushion; VS, ventricular septum.

Figure 8. Pharmacological inhibition of Dyrk1a partially rescues CHD in the Dp1Tyb mouse model of DS.

(**A**) C57BL/6J females that had been mated with Dp1Tyb males, were treated daily (vertical arrows) by oral gavage with Leucettinib-21 (LCTB-21) or iso-Leucettinib-21 (iso-LCTB-21) from 5 days after vaginal plug (VP) was found (embryonic day 0.5, E0.5). Embryos were collected at E13.5 for RNAseq, or at E14.5 for HREM. (**B**) Scatter plots comparing the $\log_2$(fold-change) (Log2FC) of mRNA expression for all genes (black) for Dp1Tyb versus WT embryos both treated with iso-LCTB-21 or Dp1Tyb embryos treated with LCTB-21 versus WT embryos treated with iso-LCTB-21. Genes from the Hallmark genesets for Oxidative Phosphorylation (left), Myc targets V1 (middle) and inflammatory response (right), are highlighted in red. *n*=5 for each condition. (**C**) Violin plots showing the Log2FC of expression of the same genesets as in B, Oxidative Phosphorylation (left), Myc targets V1 (middle), and inflammatory response (right), for the following comparisons: untreated Dp1Tyb versus WT, untreated Dp1TybDyrk1a$^{+/+/-}$ versus WT, Dp1Tyb treated with iso-LCTB-21 versus WT treated with iso-LCTB-21 and Dp1Tyb treated with LCTB-21 versus WT treated with iso-LCTB-21. Black lines indicate median, dotted lines indicate 25th and 75th centiles. Dotted line at 0 indicates no change. *n*=5 for each condition. (**D**) Graph of percentage of CHD in E14.5 mouse embryonic hearts from the indicated models. Number of hearts analyzed: WT (*n*=34) and Dp1Tyb (*n*=26) treated with iso-LCTB-21, and

Dp1Tyb treated with LCTB-21 (*n*=32). (**E**) Three copies of *Dyrk1a* and a second unknown gene (*GeneX*) lead to impaired proliferation and mitochondrial respiration in cardiomyocytes which is required for correct septation of the heart. Created in Biorender. Statistical tests were carried out with a Kruskal-Wallis (C) or Fisher's exact (D) test; * $0.01 < P < 0.05$, **** $P < 0.0001$; ns, not significant.

Figure 1

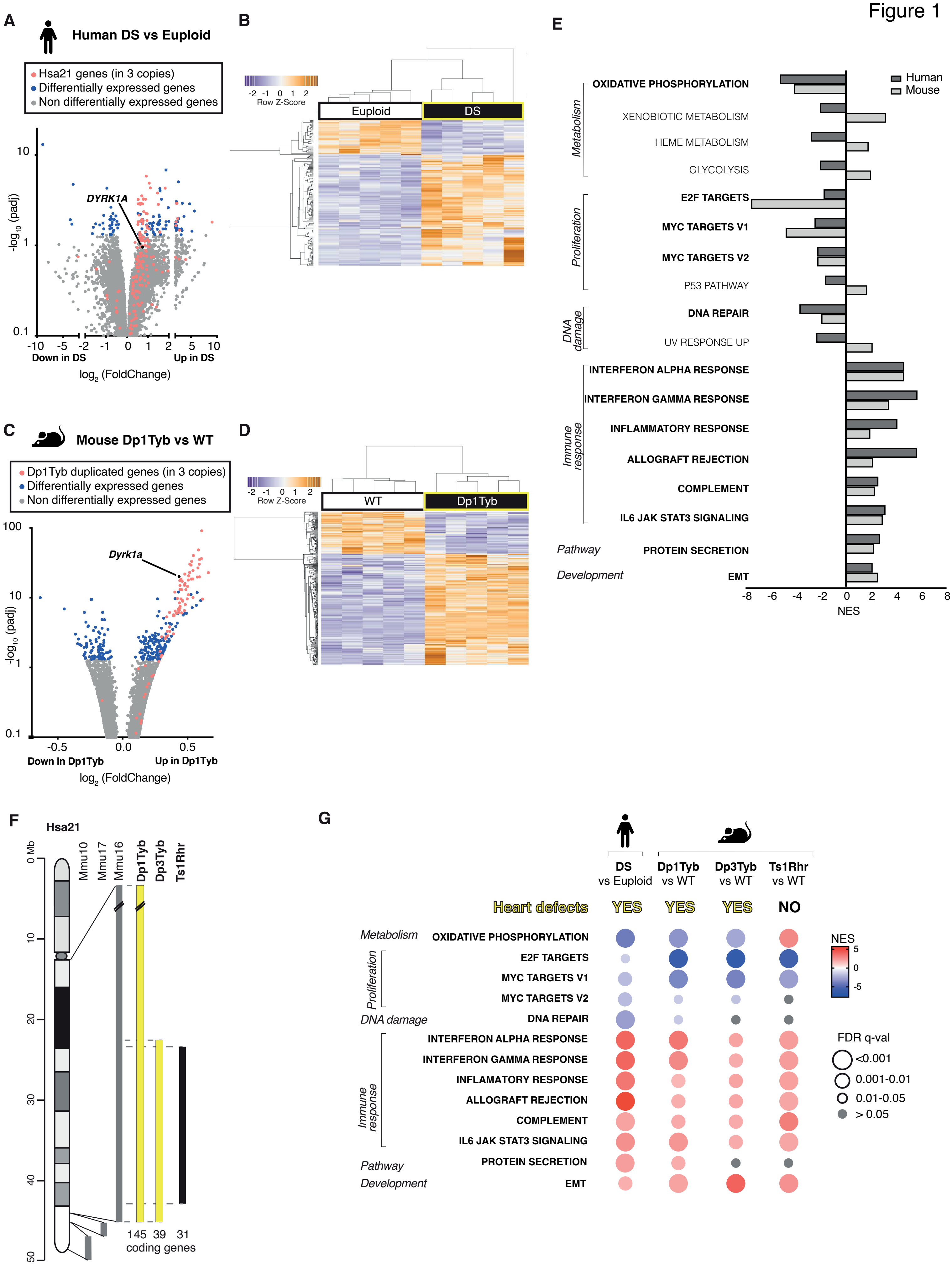
A
Human DS vs Euploid
Hsa21 genes (in 3 copies)
Differentially expressed genes
Non differentially expressed genes
-log10 (padj)
10
1
0.1
DYRK1A
-10 -5 -2 -1 0 1 2 5 10
Down in DS
Up in DS
log2 (FoldChange)
B
-2 -1 0 1 2
Row Z-Score
Euploid
DS
C
Mouse Dp1Tyb vs WT
Dp1Tyb duplicated genes (in 3 copies)
Differentially expressed genes
Non differentially expressed genes
100
10
1
0.1
-log10 (padj)
Dyrk1a
-0.5 0.0 0.5
Down in Dp1Tyb
Up in Dp1Tyb
log2 (FoldChange)
D
-2 -1 0 1 2
Row Z-Score
WT
Dp1Tyb
E
Human
Mouse
Metabolism
OXIDATIVE PHOSPHORYLATION
XENOBIOTIC METABOLISM
HEME METABOLISM
GLYCOLYSIS
Proliferation
E2F TARGETS
MYC TARGETS V1
MYC TARGETS V2
P53 PATHWAY
DNA damage
DNA REPAIR
UV RESPONSE UP
Immune response
INTERFERON ALPHA RESPONSE
INTERFERON GAMMA RESPONSE
INFLAMMATORY RESPONSE
ALLOGRAFT REJECTION
COMPLEMENT
IL6 JAK STAT3 SIGNALING
Pathway
PROTEIN SECRETION
Development
EMT
-8 -6 -4 -2 0 2 4 6 8
NES
F
Hsa21
0 Mb
10
20
30
40
50
Mmu10
Mmu17
Mmu16
Dp1Tyb
Dp3Tyb
Ts1Rhr
145 39 31
coding genes
G
DS vs Euploid
Dp1Tyb vs WT
Dp3Tyb vs WT
Ts1Rhr vs WT
Heart defects
YES
YES
YES
NO
Metabolism
OXIDATIVE PHOSPHORYLATION
Proliferation
E2F TARGETS
MYC TARGETS V1
MYC TARGETS V2
DNA damage
DNA REPAIR
Immune response
INTERFERON ALPHA RESPONSE
INTERFERON GAMMA RESPONSE
INFLAMATORY RESPONSE
ALLOGRAFT REJECTION
COMPLEMENT
IL6 JAK STAT3 SIGNALING
Pathway
PROTEIN SECRETION
Development
EMT
NES
5
0
-5
FDR q-val
<0.001
0.001-0.01
0.01-0.05
> 0.05

Figure 2

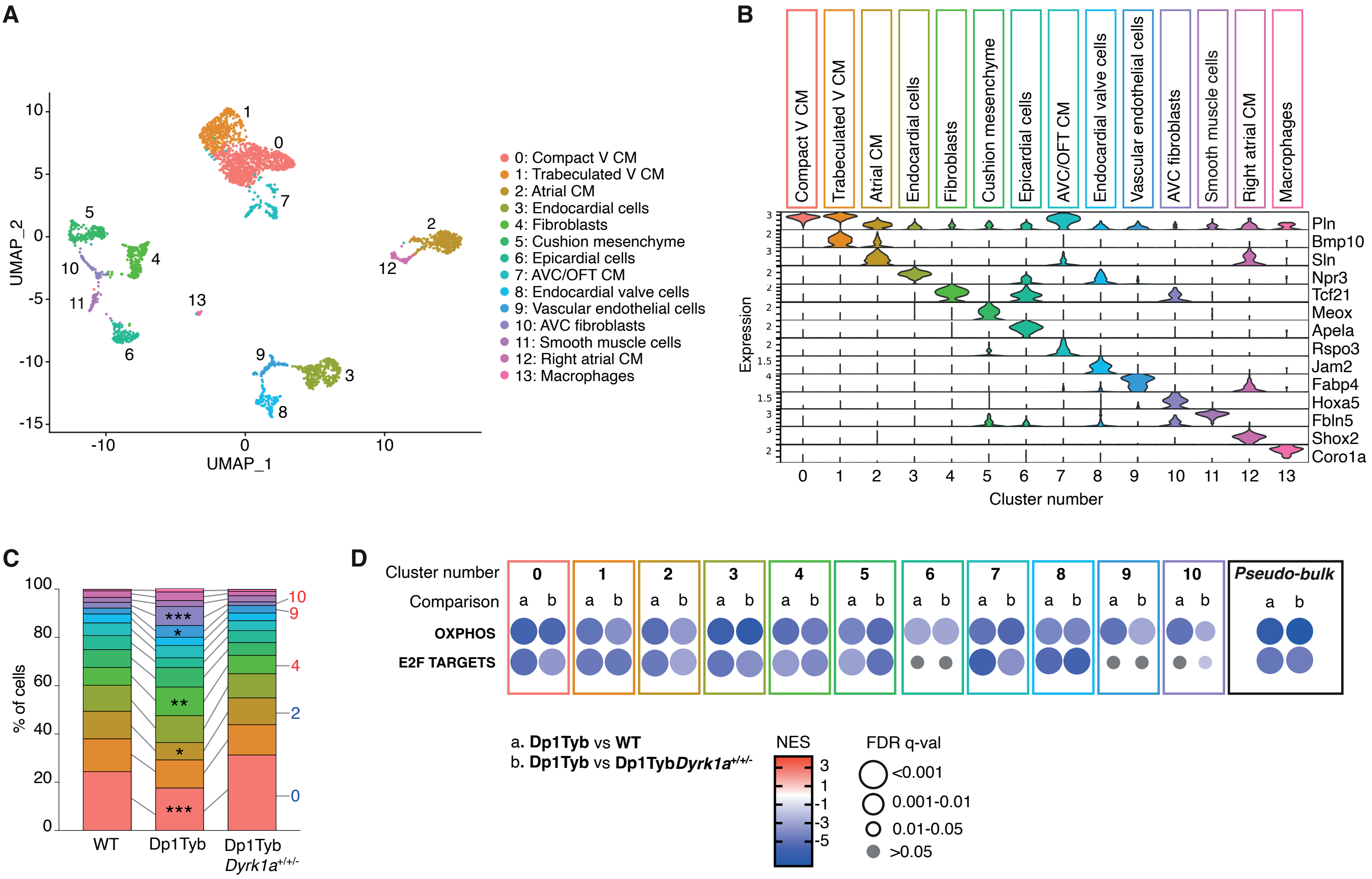
A
UMAP_2
UMAP_1
10
5
0
-5
-10
-15
-10
0
10
0: Compact V CM
1: Trabeculated V CM
2: Atrial CM
3: Endocardial cells
4: Fibroblasts
5: Cushion mesenchyme
6: Epicardial cells
7: AVC/OFT CM
8: Endocardial valve cells
9: Vascular endothelial cells
10: AVC fibroblasts
11: Smooth muscle cells
12: Right atrial CM
13: Macrophages
B
Compact V CM
Trabeculated V CM
Atrial CM
Endocardial cells
Fibroblasts
Cushion mesenchyme
Epicardial cells
AVC/OFT CM
Endocardial valve cells
Vascular endothelial cells
AVC fibroblasts
Smooth muscle cells
Right atrial CM
Macrophages
Expression
Pln
Bmp10
Sln
Npr3
Tcf21
Meox
Apela
Rspo3
Jam2
Fabp4
Hoxa5
Fbln5
Shox2
Coro1a
Cluster number
C
% of cells
100
80
60
40
20
0
***
*
**
*
***
10
9
4
2
0
WT
Dp1Tyb
Dp1Tyb Dyrk1a+/+/-
D
Cluster number
Comparison
a b
OXPHOS
E2F TARGETS
Pseudo-bulk
a. Dp1Tyb vs WT
b. Dp1Tyb vs Dp1TybDyrk1a+/+/-
NES
3
1
-1
-3
-5
FDR q-val
<0.001
0.001-0.01
0.01-0.05
>0.05

Figure 3

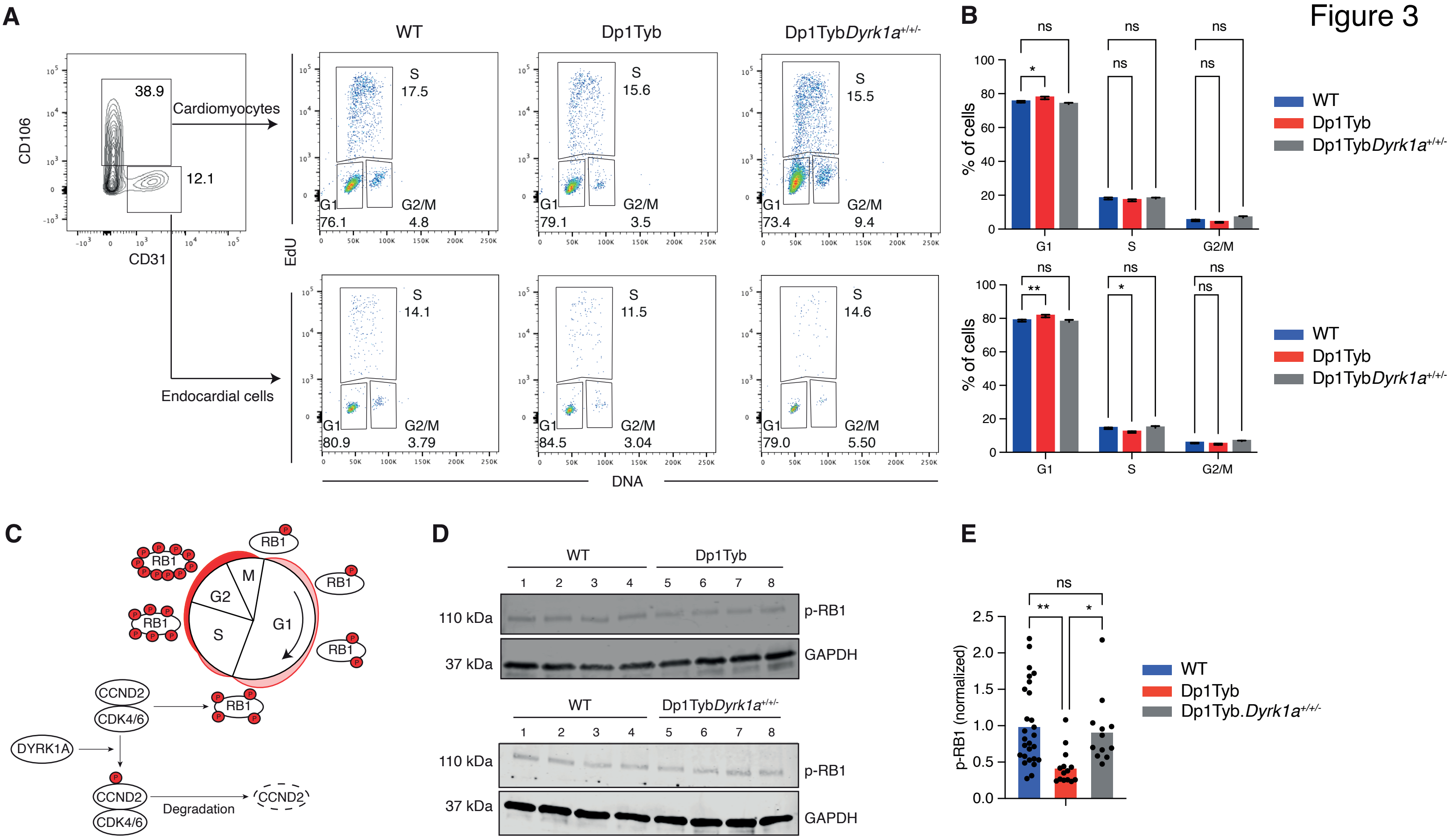
A
CD106
CD31
38.9
12.1
Cardiomyocytes
Endocardial cells
WT
Dp1Tyb
Dp1TybDyrk1a+/+/-
EdU
DNA
S
17.5
G1
76.1
G2/M
4.8
S
15.6
G1
79.1
G2/M
3.5
S
15.5
G1
73.4
G2/M
9.4
S
14.1
G1
80.9
G2/M
3.79
S
11.5
G1
84.5
G2/M
3.04
S
14.6
G1
79.0
G2/M
5.50
B
% of cells
G1
S
G2/M
ns
*
**
WT
Dp1Tyb
Dp1TybDyrk1a+/+/-
C
RB1
G2
M
S
G1
CCND2
CDK4/6
DYRK1A
Degradation
P
D
WT
Dp1Tyb
Dp1TybDyrk1a+/+/-
1 2 3 4 5 6 7 8
110 kDa
37 kDa
p-RB1
GAPDH
E
p-RB1 (normalized)
ns
**
*
WT
Dp1Tyb
Dp1Tyb.Dyrk1a+/+/-

Figure 4

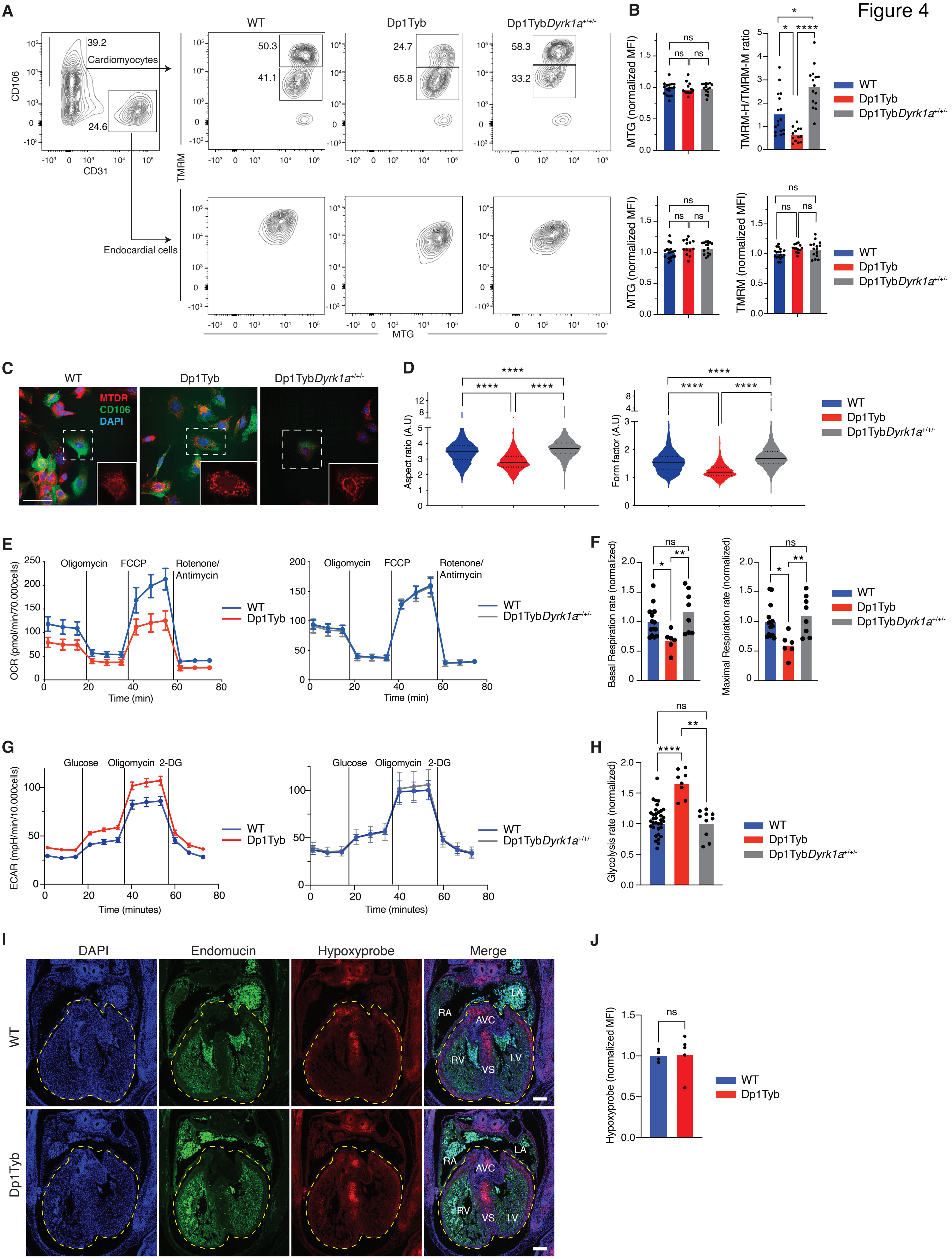
A
CD106
CD31
39.2
Cardiomyocytes
24.6
Endocardial cells
TMRM
MTG
WT
Dp1Tyb
Dp1TybDyrk1a+/+/-
50.3
41.1
24.7
65.8
58.3
33.2
B
MTG (normalized MFI)
TMRM-H/TMRM-M ratio
TMRM (normalized MFI)
ns
*
****
WT
Dp1Tyb
Dp1TybDyrk1a+/+/-
C
MTDR
CD106
DAPI
WT
Dp1Tyb
Dp1TybDyrk1a+/+/-
D
Aspect ratio (A.U)
Form factor (A.U)
****
E
OCR (pmol/min/70.000cells)
Oligomycin
FCCP
Rotenone/ Antimycin
Time (min)
WT
Dp1Tyb
Dp1TybDyrk1a+/+/-
F
Basal Respiration rate (normalized)
Maximal Respiration rate (normalized)
ns
*
**
G
ECAR (mpH/min/10.000cells)
Glucose
Oligomycin
2-DG
Time (minutes)
H
Glycolysis rate (normalized)
ns
****
**
I
DAPI
Endomucin
Hypoxyprobe
Merge
WT
Dp1Tyb
RA
LA
AVC
RV
VS
LV
J
Hypoxyprobe (normalized MFI)
ns
WT
Dp1Tyb

Figure 5

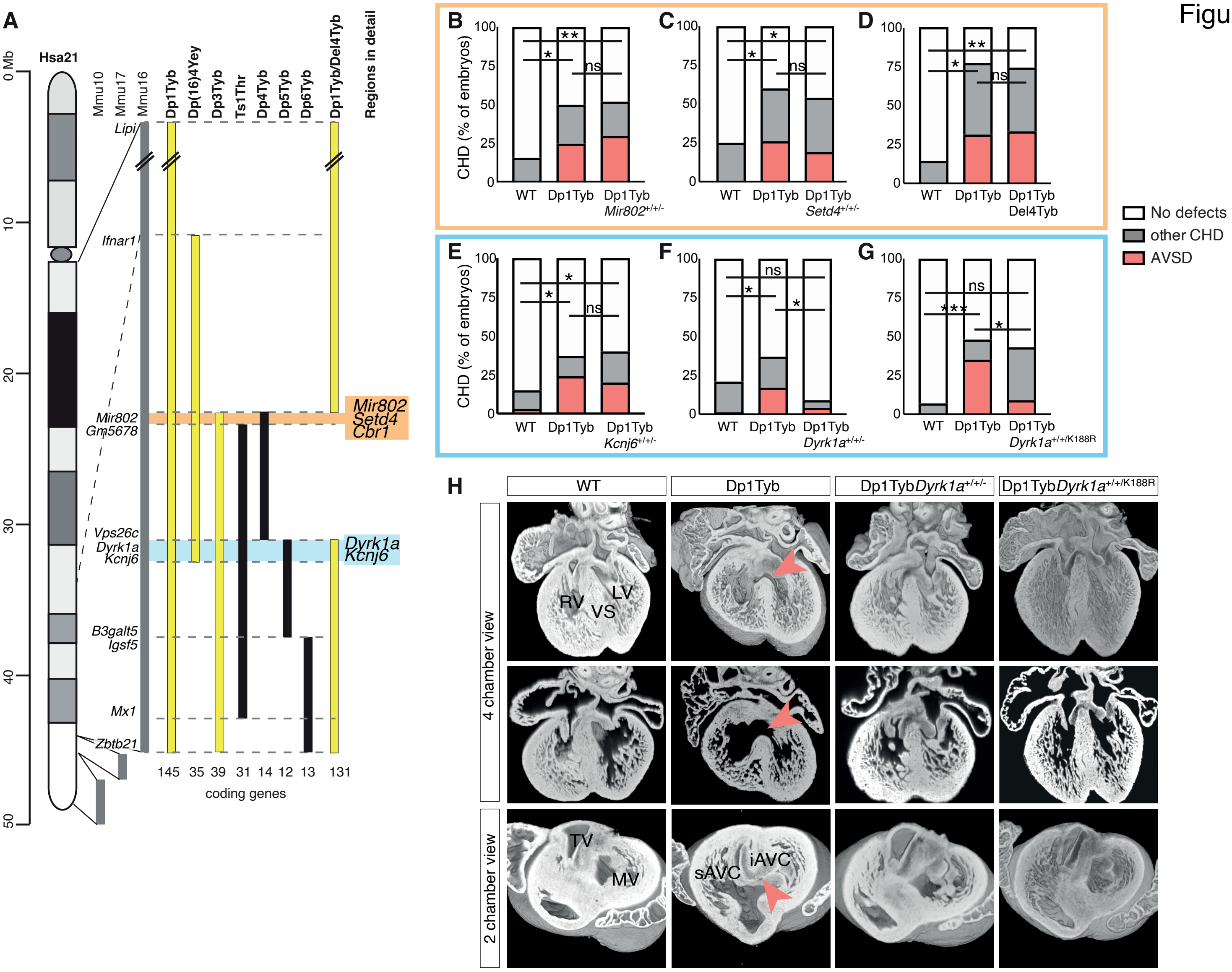
A
0 Mb
10
20
30
40
50
Hsa21
Mmu10
Mmu17
Mmu16
Dp1Tyb
Dp(16)4Yey
Dp3Tyb
Ts1Thr
Dp4Tyb
Dp5Tyb
Dp6Tyb
Dp1Tyb/Del4Tyb
Regions in detail
Lipi
Ifnar1
Mir802
Gm5678
Vps26c
Dyrk1a
Kcnj6
B3galt5
Igsf5
Mx1
Zbtb21
Mir802
Setd4
Cbr1
Dyrk1a
Kcnj6
145 35 39 31 14 12 13 131
coding genes
B
C
D
E
F
G
CHD (% of embryos)
100
75
50
25
0
WT
Dp1Tyb
Dp1Tyb Mir802+/+/-
Dp1Tyb Setd4+/+/-
Dp1Tyb Del4Tyb
Dp1Tyb Kcnj6+/+/-
Dp1Tyb Dyrk1a+/+/-
Dp1Tyb Dyrk1a+/+/K188R
*
**
***
ns
No defects
other CHD
AVSD
H
WT
Dp1Tyb
Dp1TybDyrk1a+/+/-
Dp1TybDyrk1a+/+/K188R
4 chamber view
2 chamber view
RV
LV
VS
TV
MV
sAVC
iAVC

Figure 6

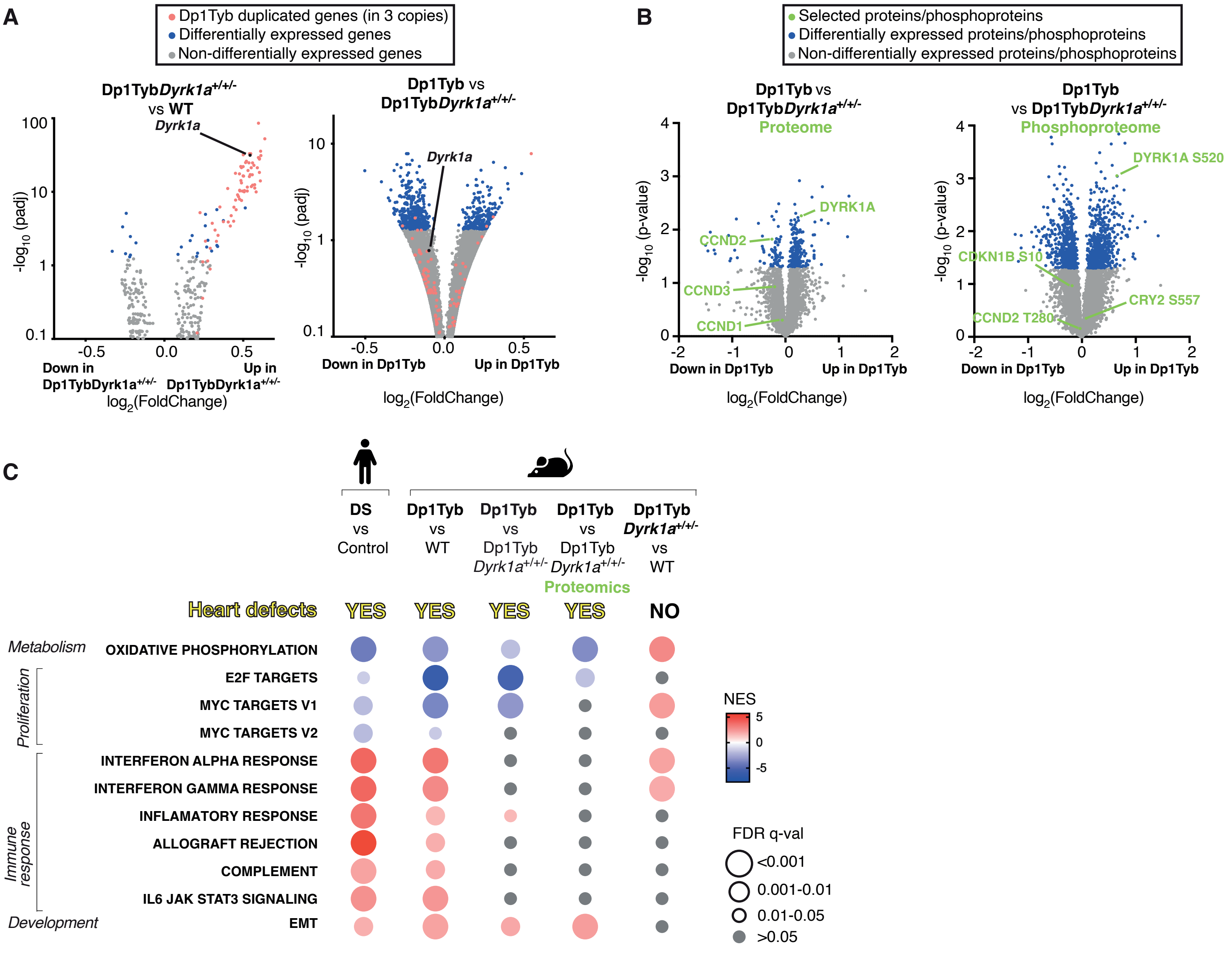
A
● Dp1Tyb duplicated genes (in 3 copies)
● Differentially expressed genes
● Non-differentially expressed genes
Dp1TybDyrk1a+/+/- vs WT
Dyrk1a
100
10
1
0.1
-log10 (padj)
-0.5
0.0
0.5
Down in Dp1TybDyrk1a+/+/-
Up in Dp1TybDyrk1a+/+/-
log2(FoldChange)
Dp1Tyb vs Dp1TybDyrk1a+/+/-
Dyrk1a
10
1
0.1
-log10 (padj)
-0.5
0.0
0.5
Down in Dp1Tyb
Up in Dp1Tyb
log2(FoldChange)
B
● Selected proteins/phosphoproteins
● Differentially expressed proteins/phosphoproteins
● Non-differentially expressed proteins/phosphoproteins
Dp1Tyb vs Dp1TybDyrk1a+/+/-
Proteome
DYRK1A
CCND2
CCND3
CCND1
4
3
2
1
0
-log10 (p-value)
-2
-1
0
1
2
Down in Dp1Tyb
Up in Dp1Tyb
log2(FoldChange)
Dp1Tyb vs Dp1TybDyrk1a+/+/-
Phosphoproteome
DYRK1A S520
CDKN1B S10
CRY2 S557
CCND2 T280
4
3
2
1
0
-log10 (p-value)
-2
-1
0
1
2
Down in Dp1Tyb
Up in Dp1Tyb
log2(FoldChange)
C
DS vs Control
Dp1Tyb vs WT
Dp1Tyb vs Dp1Tyb Dyrk1a+/+/-
Dp1Tyb vs Dp1Tyb Dyrk1a+/+/-
Proteomics
Dp1Tyb Dyrk1a+/+/- vs WT
Heart defects
YES
YES
YES
YES
NO
Metabolism
OXIDATIVE PHOSPHORYLATION
Proliferation
E2F TARGETS
MYC TARGETS V1
MYC TARGETS V2
Immune response
INTERFERON ALPHA RESPONSE
INTERFERON GAMMA RESPONSE
INFLAMATORY RESPONSE
ALLOGRAFT REJECTION
COMPLEMENT
IL6 JAK STAT3 SIGNALING
Development
EMT
NES
5
0
-5
FDR q-val
<0.001
0.001-0.01
0.01-0.05
>0.05

Figure 7

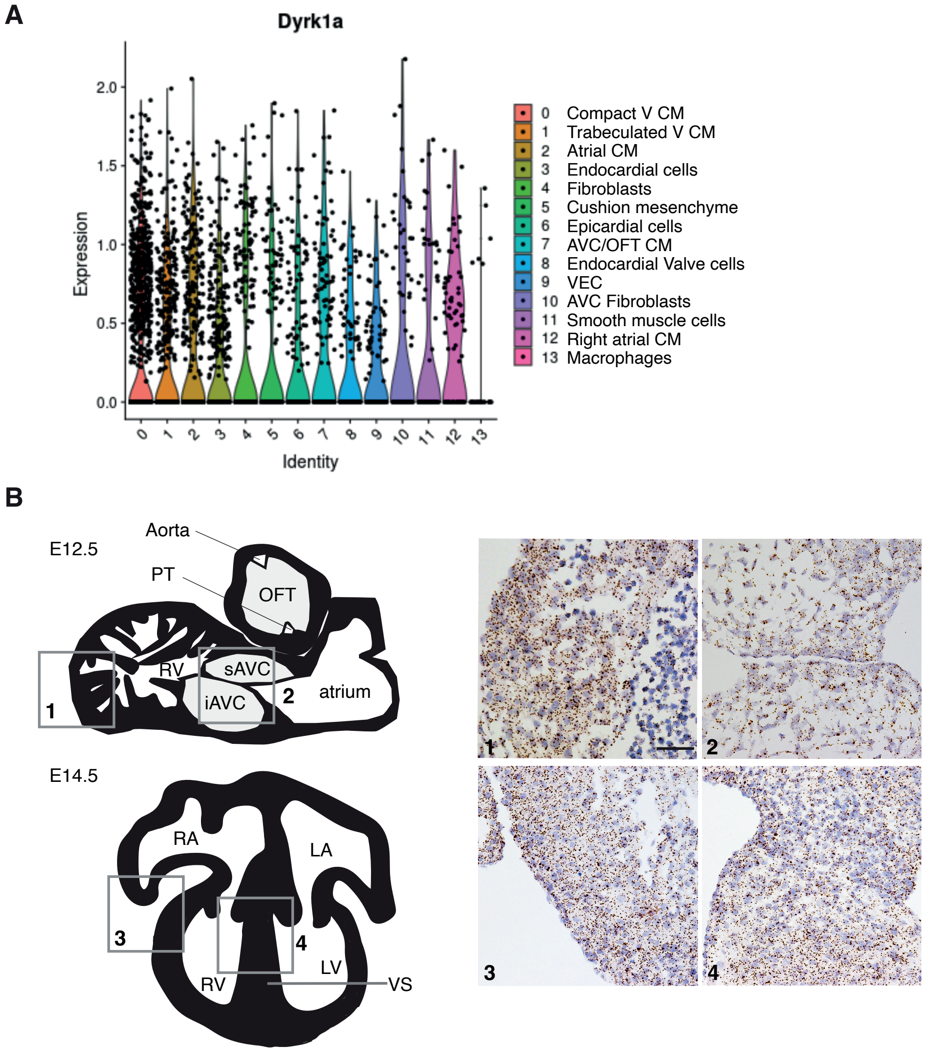
A
Dyrk1a
Expression
2.0
1.5
1.0
0.5
0.0
0
1
2
3
4
5
6
7
8
9
10
11
12
13
Identity
0 Compact V CM
1 Trabeculated V CM
2 Atrial CM
3 Endocardial cells
4 Fibroblasts
5 Cushion mesenchyme
6 Epicardial cells
7 AVC/OFT CM
8 Endocardial Valve cells
9 VEC
10 AVC Fibroblasts
11 Smooth muscle cells
12 Right atrial CM
13 Macrophages
B
E12.5
Aorta
PT
OFT
RV
sAVC
iAVC
atrium
1
2
E14.5
RA
LA
3
4
RV
LV
VS
1
2
3
4

Figure 8

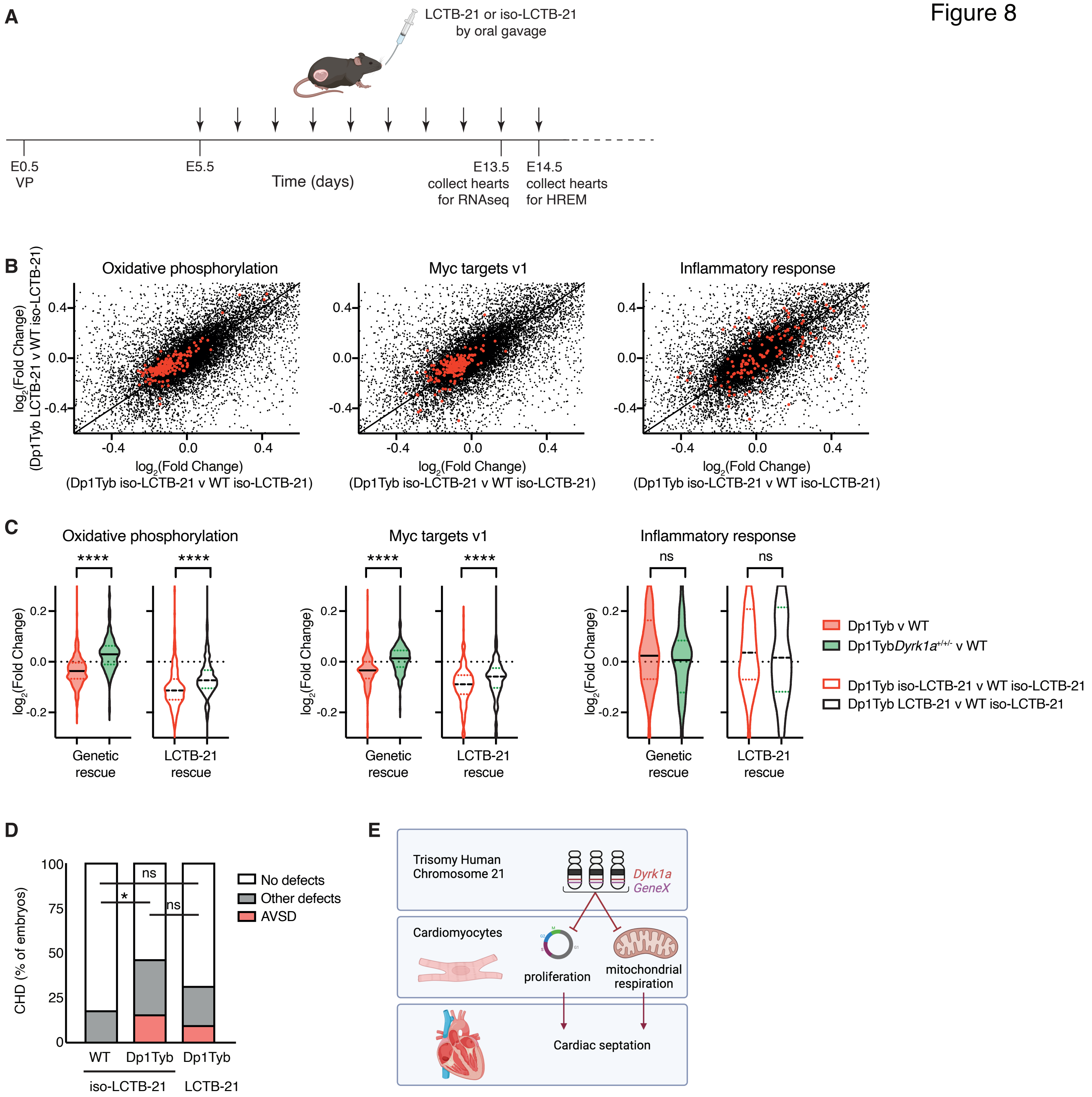
A
LCTB-21 or iso-LCTB-21
by oral gavage
E0.5
VP
E5.5
Time (days)
E13.5
collect hearts
for RNAseq
E14.5
collect hearts
for HREM
B
Oxidative phosphorylation
Myc targets v1
Inflammatory response
log2(Fold Change)
(Dp1Tyb LCTB-21 v WT iso-LCTB-21)
log2(Fold Change)
(Dp1Tyb iso-LCTB-21 v WT iso-LCTB-21)
0.4
0.0
-0.4
C
Oxidative phosphorylation
Myc targets v1
Inflammatory response
****
ns
log2(Fold Change)
0.2
0.0
-0.2
Genetic
rescue
LCTB-21
rescue
Dp1Tyb v WT
Dp1TybDyrk1a+/+/- v WT
Dp1Tyb iso-LCTB-21 v WT iso-LCTB-21
Dp1Tyb LCTB-21 v WT iso-LCTB-21
D
CHD (% of embryos)
100
75
50
25
0
ns
*
ns
No defects
Other defects
AVSD
WT
Dp1Tyb
Dp1Tyb
iso-LCTB-21
LCTB-21
E
Trisomy Human
Chromosome 21
Dyrk1a
GeneX
Cardiomyocytes
proliferation
mitochondrial
respiration
Cardiac septation

Increased dosage of DYRK1A leads to congenital heart defects in a mouse model of Down syndrome

Supplementary Materials and Methods

Array Comparative Genome Hybridization (aCGH)

Genomic DNA was prepared from tails of Del4Tyb (test) and C57BL/6J (control) mice. DNA, labeled with Cy3 (test) and Cy5 (control), was hybridized by Roche Diagnostics Limited to a mouse 3x720K array (Roche NimbleGen) containing 50-75mer probes designed based on mouse genome assembly MGSCv37. The hybridized aCGH slides were scanned in the Cy3 and Cy5 channels. The Log2 ratios of the test/control signals were calculated for all probes and the ratios for the probes on Mmu16 were plotted in genomic order to visualize the deleted region.

RNA sequencing (RNAseq)

Frozen human fetal hearts (13-14 pcw, 5 DS and 5 euploid age- and sex-matched samples) were obtained from the MRC-Wellcome Trust Human Developmental Biology Resource (HDBR). Frozen tissues were placed in RLT lysis buffer (Qiagen) in gentleMACS M-tubes (Miltenyi Biotec), homogenized using the gentleMACS Octo dissociator (Miltenyi Biotec) and RNA was extracted using the RNAeasy Maxi kit (Qiagen). RNA integrity numbers (RIN) of the samples were 7-9.4. Stranded polyA-enriched libraries were made using the KAPA mRNA HyperPrep kit (Roche) according to the manufacturer's instructions and sequenced on the HiSeq 4000 (Illumina) with single-ended 100 base reads. An average of 34 million reads were generated per sample.

E13.5 mouse hearts from Dp1Tyb, Dp1Tyb*Dyrk1a*$^{+/+/-}$, Dp3Tyb and Ts1Rhr embryos and WT littermate embryos for each strain (5 per genotype) were dissected and snap frozen. Frozen tissues were placed in lysis buffer and homogenized using a cordless Pellet pestle (Sigma-Aldrich) followed by RNA extraction using RNAeasy mini kit (Qiagen). RNA integrity numbers (RIN) of the samples were 9.8-10. Stranded polyA-enriched libraries were made using the KAPA mRNA HyperPrep kit (Roche) according to the manufacturer's instructions and sequenced on the HiSeq 2500 or HiSeq 4000 (Illumina) with single ended 100 base reads. An average of 24 million reads were generated for the Dp1Tyb and Dp1Tyb*Dyrk1a*$^{+/+/-}$ and WT samples and an average of 34 million reads for Dp3Tyb, Ts1Rhr and corresponding WT samples. Adaptor trimming was performed with Trimmomatic/0.36-Java-1.7.0_80 with parameters "LEADING:3 TRAILING:3 SLIDINGWINDOW:4:20 MINLEN:36" (*62*). The RSEM package (v.1.2.31) in conjunction with the STAR alignment algorithm (v.2.5.2a) was used for the read mapping and gene-level quantification with respect to mouse genome assembly GRCm38 (release 86) for the mouse data sets and human genome assembly GRCh38 (release 89) for the human samples (*63, 64*). Unsupervised hierarchical clustering was carried out using Euclidean distance with the heatmap.2 function from gplots (*65*). Differential expression analysis was performed with the DESeq2 package within the R programming environment (*66, 67*). The significance threshold for the identification of differentially expressed genes was set as an adjusted *P* value ≤0.05. Gene set enrichment analysis was carried out with the GSEA software (version 2.2.3) (*10*). The software compares ranked lists of genes, in this case, differentially expressed genes ranked by the "stat" value in decreasing order, with the following gene sets from the Molecular Signature Database: "c2.cp.v7.0.symbols.gmt", "c5.bp.v7.0.symbols.gmt", "h.all.v7.0.symbols.gmt" downloaded from the Broad Institute (http://www.broad.mit.edu/gsea/). GSEAPreranked was used with "classic" enrichment analysis not excluding large datasets.

For the pharmacological rescue experiment, 5 E13.5 hearts were analyzed for each of the 4 conditions: 2 genotypes (WT and Dp1Tyb) x 2 treatments (LCTB-21 and iso-LCTB-21). Both male and female embryos were analyzed, with the same numbers of each sex in each of the 4 groups. Samples were dissected and snap frozen. Frozen tissues were placed in lysis buffer and homogenized using a cordless Pellet pestle (Sigma-Aldrich) followed by RNA extraction using RNAeasy micro kit (Qiagen). RNA integrity numbers (RIN) of the samples were 10. Stranded polyA enriched libraries were generated using NEBNext Ultra II Directional RNA Library Prep Kit for Illumina according to manufacturer's instructions. An average of 25 million paired end reads per library (PE100) were generated on a NovaSeq6000 (Illumina). All samples were processed using the nf-core RNAseq pipeline (v.3.10.1) operating on Nextflow (v.22.10.3) (*68, 69*). Settings for individual tools were left as standard for this workflow version unless otherwise specified. Alignment to GRCm38 (release 95) was performed using STAR (v2.7.10a) (*64*), followed by quantification using RSEM (v1.3.1) (*63*). Results were further processed in R (version 4.2.0) (*67*). Outputs of the RNAseq pipeline were assessed for quality using the metrics provided by the pipeline's inbuilt quality control packages, PCA (package stats v4.2.0), and correlation analyses between samples (package stats v4.2.0). Differential expression analysis was performed with DESeq2 (v1.38.3) (*66*), using a model accounting for differences in litter, sex, treatment and genotype (~ *litter* + *sex* + *treatment* * *genotype*). The significance threshold for the identification of differentially expressed genes was set as an adjusted *P* value ≤0.05, where *P* values were adjusted for false discovery rates according to the Independent Hypothesis Weighting method (package IHW, v1.26.0) (*70, 71*). Bulk RNAseq data have been deposited in the Gene Expression Omnibus, accession codes: GSE196447 and GSE239798.

Single cell RNAseq

E13.5 mouse hearts from Dp1Tyb, Dp1Tyb*Dyrk1a*$^{+/+/-}$ and WT littermate embryos were dissected and subsequently dissociated into single cells using the Neonatal Heart Dissociation kit and gentleMACS Octo dissociator (Miltenyi Biotec). Cells in suspension were methanol fixed, filtered through a 30 µm cell strainer, spun down and stored at -20ºC. Fixed cells were resuspended in PBS, 0.04% BSA, assessed for viability using trypan blue staining and quantified using the EVE automated cell counter (Cambridge Bioscience). Cells were processed using the Chromium 3' mRNA-Seq version 2 kit (10x Genomics). Samples were sequenced on the HiSeq 4000 acquiring at least 142,000 reads per cell, achieving a sequencing saturation of 73 - 90%.

Cell Ranger software (version 2.1.1, 10x Genomics) was used to de-multiplex Illumina BCL output, create fastq files and generate single cell feature counts for each library using GRCm38 (v1.2.0) as reference. All subsequent analyses were performed in R (v3.6.1) using the Seurat (v 3.1) package (*67, 72*). Genes were removed if they were expressed in 3 or fewer cells and cells with < 200 expressed genes detected were also removed. After quality control and filtering 3,384 cells were retained for further analysis. Data was integrated following Seurat's vignette. In brief, for each sample the top 2000 most variable genes were selected for data integration using Canonical correlation Analysis (CCA) with 50 dimensions for dimensional reduction using tSNE and cluster calling using the Louvain algorithm. Clusters were visualized using the Uniform Manifold Approximation and Projection (UMAP). Upon initial examination of the clusters, we detected small clusters corresponding to red blood cells and lung tissue, both of which were removed. Subsequently data was normalized and integrated, and clustering analysis was repeated with the same parameters as above, with the addition that the effects of cell cycle were regressed out. A cluster resolution of 0.4 was used to define clusters for further analysis.

Cluster markers were identified using "FindConservedMarkers" with default parameters. Differentially expressed genes within each cluster were identified using the DESeq2 test in "FindMarkers" using data in which the effects of cell cycle had not been regressed out. scRNAseq data have been deposited in the Gene Expression Omnibus, accession code: GSE196447.

Proteomics

E13.5 mouse hearts from Dp1Tyb*Dyrk1a*$^{+/+/-}$ and WT littermate embryos (5 per genotype) were dissected, snap frozen and stored at -80ºC. Frozen tissues were placed in 8M Urea with phosSTOP protease inhibitors (Roche) and homogenized using a cordless Pellet pestle (Sigma-Aldrich). Lysates were reduced, alkylated and digested with tryspin using standard methods. Nest Group C_{18} MacroSpin columns (SMMSS18V) were used to concentrate and clean up the peptides according to the manufacturer supplied instructions, prior to labeling with TMT10plex Isobaric Label Reagent Set (ThermoFisher Scientific). TMT-labeled samples were pooled, enriched for phospho-peptides using the High-Select Fe-NTA phosphopeptide enrichment kit (A32992, ThermoFisher Scientific) and using Titansphere TiO 5 μm bulk media (GL Sciences) according to the manufacturer supplied protocols. Samples were analyzed by LC-MS/MS on an Orbitrap Fusion Lumos Mass Spectrometer (ThermoFisher Scientific). Raw data were processed in MaxQuant v1.6.0.13 (https://www.maxquant.org/), with the database search conducted against the canonical sequences of the UniProt Mus Musculus complete proteome, downloaded August 2017. Statistical analysis was carried out using Perseus (https://www.maxquant.org/perseus/). In brief, abundance values for each protein were log2 transformed, median normalized and a Welch t-test was used to evaluate the significance of differences between samples of the two genotypes, generating an FDR corrected p-value and log2(fold change of the geometric means). The mass spectrometry proteomics data have been deposited with the ProteomeXchange Consortium (http://proteomecentral.proteomexchange.org) through the PRIDE partner repository (*73*), dataset identifier PXD013053.

HREM imaging and 3D modeling

E14.5 embryonic hearts were dissected and fixed for 30 min in 4% paraformaldehyde followed by a 1 h wash in distilled water and fixed a second time overnight. Fixed samples were dehydrated and embedded in modified JB4 methacrylate resin (*74*). Samples were sectioned at 2.5 μm and imaged using a Jenoptik camera with an isometric resolution of 2 μm. Data sets were normalized and subsampled prior to 3D volume rendering using OsiriX MD (*75*). Phenotype analysis was performed blind for genotype and classification of type of CHD was carried out as previously described (*76*). Mutant and control WT hearts were taken from the same litters.

Flow cytometry

E13.5 mouse hearts from Dp1Tyb and WT littermate embryos and Dp1Tyb*Dyrk1a*$^{+/+/-}$ and their WT littermates were dissociated into single cells using the Neonatal Heart Dissociation kit and gentleMACS Octo dissociator (Miltenyi Biotec). To evaluate mitochondrial membrane potential and content cells in suspension were incubated with 20 nM tetramethylrhodamine methyl ester (TMRM, Thermo Fisher) and 20 nM of Mitotracker Green (MTG, Thermo Fisher), respectively, for 30 min at 37°C. Cells were then stained with anti-CD106-APC, anti-CD31-BV785 and Zombie Aqua (all Biolegend, 105718, 102435, 423102, respectively). CD106 (VCAM-1) is predominantly expressed on cardiomyocytes in mouse embryonic hearts (*77*). CD31 (PECAM1) is expressed on both endocardial and endothelial cells, but in E13.5 hearts most CD31^{+} cells are endocardial cells (Figure 2C). Zombie Aqua was used to distinguish live and dead cells. To analyze cell cycle phases, dissected E13.5 mouse hearts were incubated with 10 µM EdU at 37°C for 30 min, and then dissociated into single cells using the Neonatal Heart Dissociation kit and gentleMACS Octo dissociator (Miltenyi Biotec). Cells in suspension were stained in PBS with anti-CD106-APC, anti-CD31-BV785 (Biolegend) and Live/dead Near-IR (ThermoFisher, L10119) for 30 min, followed by fixation in 4% Paraformaldehyde (PFA) for 20 min. EdU was detected using the Click-it EdU kit (Life Technologies), and DNA was stained with FxCycle violet (ThermoFisher). Data were acquired on an LSR Fortessa X-20 cell analyzer (BD) and analyzed using FlowJo v9.

Immunoblot analysis

E13.5 mouse hearts from Dp1Tyb and WT littermate embryos were dissected and snap frozen. Frozen tissues were placed in RIPA lysis buffer and homogenized using a cordless Pellet pestle (Sigma-Aldrich) followed by protein extraction. Total protein lysates (20 µg) were resolved on a denaturing 4-10% precast SDS-PAGE (Bio-Rad) and probed with rabbit monoclonal antibodies against phospho-RB1 (Ser807/Ser811) and GAPDH (Cell Signaling Technology, 8516 and 5174, respectively). Binding of primary antibodies was detected using AF680–conjugated anti-rabbit IgG (Thermo Fisher Scientific). Fluorescence from the secondary reagents was detected using an Odyssey (LI-COR Biosciences). For quantitation, signal from phospho-RB1 was normalized to GAPDH.

Metabolic analysis

E13.5 mouse hearts from Dp1Tyb and WT littermate embryos and Dp1Tyb*Dyrk1a*$^{+/+/-}$ and their WT littermates were dissociated into single cells as described above. To measure rates of mitochondrial respiration, cells were seeded onto Seahorse 8-well plates in in XF D-MEM Medium pH 7.4 containing 10 mM glucose, 2 mM L-glutamine and 1 mM sodium pyruvate (all Agilent Technologies). The plates were centrifuged at 100xg for 3 min, kept at 37°C for 45-60 min and the oxygen consumption rate (OCR) was measured using a Seahorse XFp Analyzer (Agilent Technologies). To investigate mitochondrial respiration phenotypes, a Seahorse XFp Cell Mito Stress Test kit (Agilent Technologies) was used. Cells were analyzed for 20 min and then oligomycin (1 μM, final concentration) was added, followed by carbonyl cyanide 4-(trifluoromethoxy) phenylhydrazone (FCCP) (1 μM, final concentration) 20 min later, and rotenone and antimycin A (0.5 μM, final concentration) a further 20 min after that. To measure glycolysis, cells were seeded onto Seahorse 96-well plates in in XF D-MEM Medium pH 7.4 containing 2 mM L-glutamine. The plates were centrifuged at 100xg for 3 min, kept at 37°C for 45-60 min and the extra-cellular acidification rate (ECAR) was measured using a Seahorse XFe96 Analyzer, using a Seahorse XFe96 Glycolysis stress Test kit (Agilent Technologies). To establish the basal ECAR, ECAR was measured for 20 min at the beginning of the assay. After 20 min, glucose (10 mM) was added, followed by oligomycin (1 μM) 20 min later, and 2-deoxy-D-glucose (50 mM) a further 20 min after that. Cells were fixed with 4% PFA for 15 min, nuclei were stained with 4′,6-diamidino-2-phenylindole (DAPI) and imaged using an EVOS microscope (Thermo Fisher). The Analyze Particles command from ImageJ was used to calculate numbers of nuclei which were used to normalize the OCR and ECAR data to numbers of cells in a well. Further analysis of OCR and ECAR was carried out using WAVE (version 2.6.1, Agilent Technologies).

Mitochondrial shape analysis

E13.5 mouse hearts from Dp1Tyb and WT littermate embryos and Dp1Tyb*Dyrk1a*$^{+/+/-}$ and their WT littermates were dissociated as previously described. Cells were seeded on 96-well plates (Greiner Bio-One) and cultured overnight to allow them to adhere. Mitochondria were stained by incubating the cells with 20 nM of MitoTracker Deep Red (MTDR) for 30 min at 37°C and fixed with 2% PFA for 20 min at 37°C. Cells were stained with rat antimouse CD106 (BD Bioscience) overnight at 4°C, followed by goat anti-rat IgG Alexa Fluor 488 (Thermo Fisher) for 1 h at room temperature, and DAPI for 10 min at room temperature. Cells were imaged with the Opera Phenix High-Content Screening System (PerkinElmer). Initially, images were acquired using PreciScan imaging with a x20/NA 0.4 air lens and the locations of single cardiomyocytes (CD106$^+$) were defined using Harmony software V4.9. Next, single cardiomyocytes were re-imaged using a x63/NA 1.15 water-immersion lens. Z-stacks from 0 to 3 µm with a step size of 1 µm were acquired using excitation lasers at 405 nm (DAPI), 488 nm (anti-CD106) and 640 nm (MTDR). The mitochondrial network was identified using the MTDR signal (mitochondria) transformed into Ridge texture using the SER (Saddles, Edges, Ridges) feature of Harmony V4.9 (PerkinElmer). Mitochondrial shape was assessed using aspect ratio (major axis length/minor axis length), a measure of the length to width ratio, and form factor (perimeter^2/4π[area]), reflecting the complexity and branching of mitochondria (*54*). These parameters were determined using Harmony software on maximum projection images (fig. S3A, B).

Hypoxia analysis

E13.5 pregnant mice were injected i.p. with 60 mg/kg of Hypoxyprobe-1 (pimonidazole HCl, Hypoxyprobe, Inc.) in saline. Embryonic hearts were dissected 2 to 3 h post injection and fixed for 15 min in 4% paraformaldehyde followed by 1 h wash in distilled water and fixed a second time overnight. Hearts were paraffin-embedded and sectioned at 4 µm thickness and mounted on SuperFrost Plus slides. Hypoxyprobe was detected using a rabbit anti-pimonidazole antibody from the Hypoxyprobe Omni-Kit (Hypoxyprobe, Inc.), mouse anti-cardiac troponin (MA5-12960, Thermo Scientific) and rat anti-endomucin (Sc-65495, Santa Cruz) overnight at 4°C, followed by goat anti-rabbit IgG Cy3, goat antimouse IgG AF647 and goat anti-rat IgG AF488 (Thermo Fisher) for 1 h at room temperature, and DAPI for 10 min at room temperature.

RNAscope

E12.5 mouse embryos and E14.5 dissected hearts were fixed in 10% neutral buffered formalin for 24 h, dehydrated, embedded in paraffin, and sectioned sagittally or frontally, respectively. Expression of *Dyrk1a* RNA on the sections was detected using ACD RNAscope 2.5 HD Assay - BROWN with a probe targeting the *Dyrk1a* gene (325-1455 bp, ACD catalogue number 432191) according to manufacturer's instructions. Slides were counterstained with haematoxylin.

Treatment of pregnant mice with Leucettinib-21

C57BL/6J female mice were mated with C57BL/6J males. From 5 days post coitum (E5.5), pregnant mice were orally gavaged daily with 0.3, 3 or 30 mg/kg of Leucettinib-21 (Figure S5A, Perha Pharmaceuticals) in 0.5% carboxymethylcellulose sodium salt (Sigma 9004-32-4) until E14.5. Embryos were dissected 2 h after the final gavage, snap frozen and then analyzed by mass spectrometry for the presence of Leucettinib-21 (Oncodesign Services). Alternatively, C57BL/6J female mice were mated with Dp1Tyb males and pregnant mice were treated with 30 mg/kg of Leucettinib-21 or iso-Leucettinib-21 in 0.5% carboxymethylcellulose daily by oral gavage from E5.5 to E13.5 (for RNAseq) or E14.5 (for HREM). Embryonic hearts were dissected 2h after the final gavage and processed for RNAseq and HREM imaging as described above.

Supplementary Figures

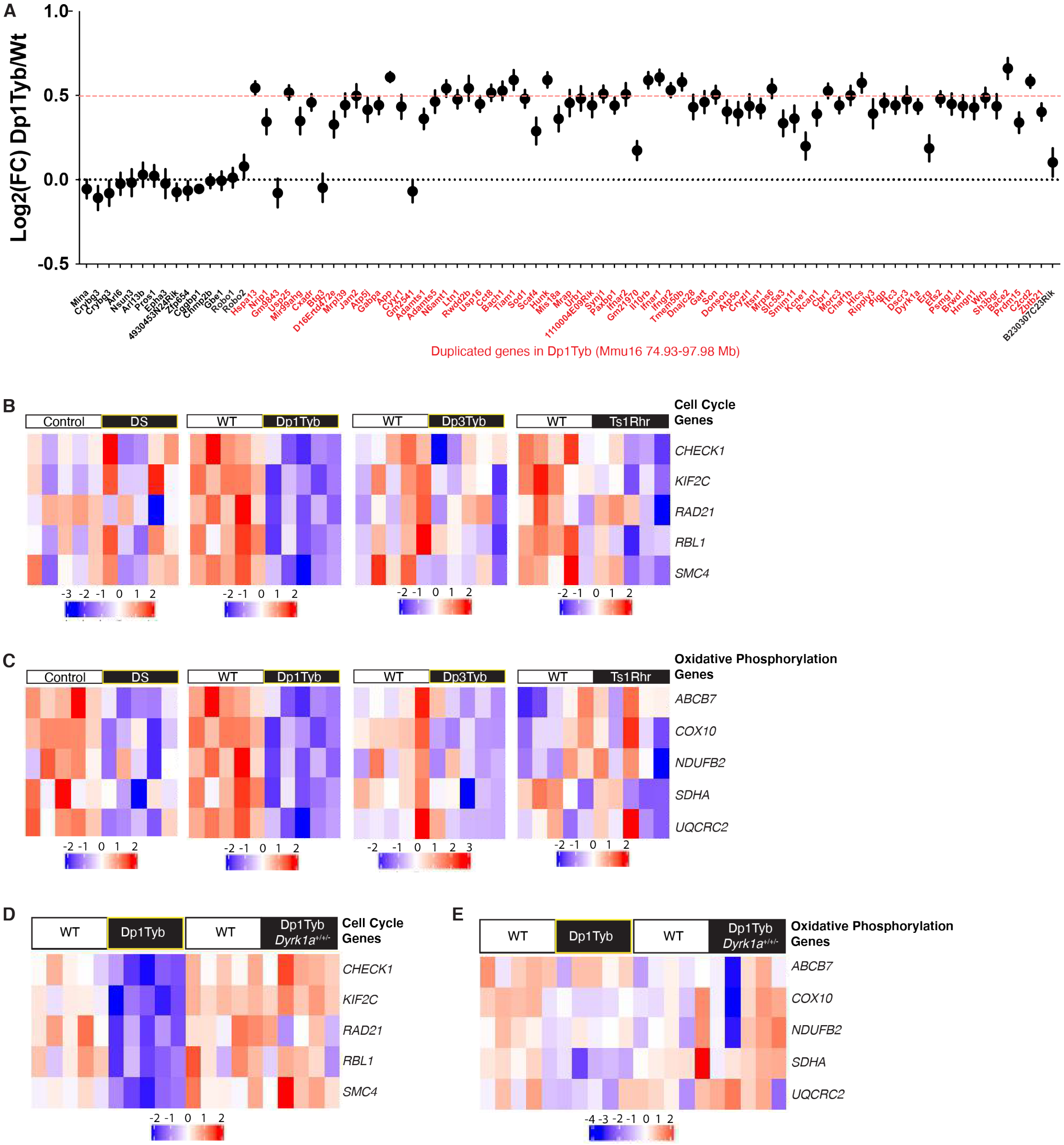

Figure S1. Altered gene expression in DS and Dp1Tyb embryonic hearts.

(**A**) Mean±SEM $\log_2$(fold-change) of gene expression between WT and Dp1Tyb E13.5 hearts (*n*=5). Only expressed genes are shown, defined as genes whose mean expression is >5 TPM and having a measured *P*-value in DEseq2. Genes within the duplicated region of Mmu16 are shown in red. For comparison, 15 genes that are centromeric to this region of Mmu16 and one gene telomeric to this region and not duplicated are shown in black. Dashed red line indicates a fold change of 1.5 expected by the increased dosage of the duplicated genes; dotted black line represents no change in expression. All but three of the duplicated genes show increased expression. FC, fold-change. (**B-E**) Heatmaps showing change in gene expression of selected genes from (B, D) the Reactome cell cycle and (C, E) Hallmark oxidative phosphorylation gene sets in (B, C) DS and control euploid human embryonic hearts, and in Dp1Tyb, Dp3Tyb and Ts1Rhr mouse E13.5 hearts and their corresponding WT controls and (D, E) in Dp1Tyb and Dp1Tyb*Dyrk1a*$^{+/+/-}$ embryonic hearts and their corresponding WT littermate controls. Red and blue colors indicate increased or decreased expression of indicated genes relative to the mean expression of each row using normalized $\log_2$ expression values.

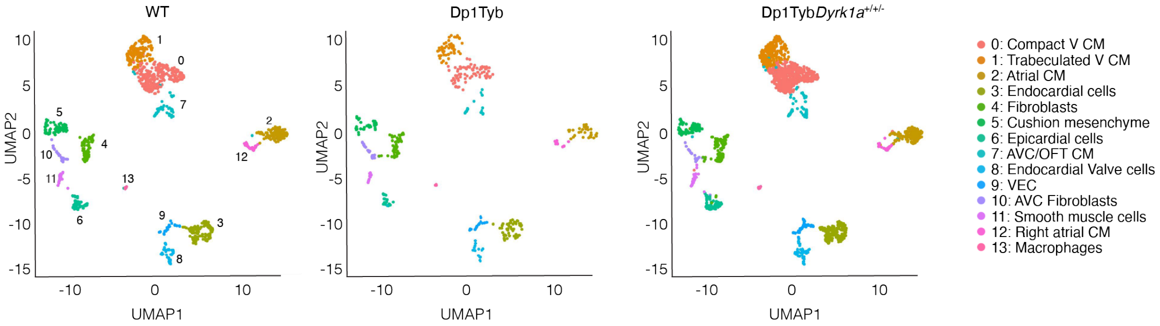

Figure S2. scRNAseq analysis of Dp1Tyb and Dp1Tyb *Dyrk1a*$^{+/+/-}$ embryonic hearts. UMAP plots of scRNAseq data from WT, Dp1Tyb and Dp1Tyb *Dyrk1a*$^{+/+/-}$ mouse E13.5 embryonic hearts. Clusters were generated by pooling data from all hearts and all genotypes as shown in Figure 2A. The plots in this figure use the same clustering but show cells in each genotype separately. Sample numbers: *n*=2 WT, 1 Dp1Tyb, 2 Dp1Tyb*Dyrk1a*$^{+/+/-}$.

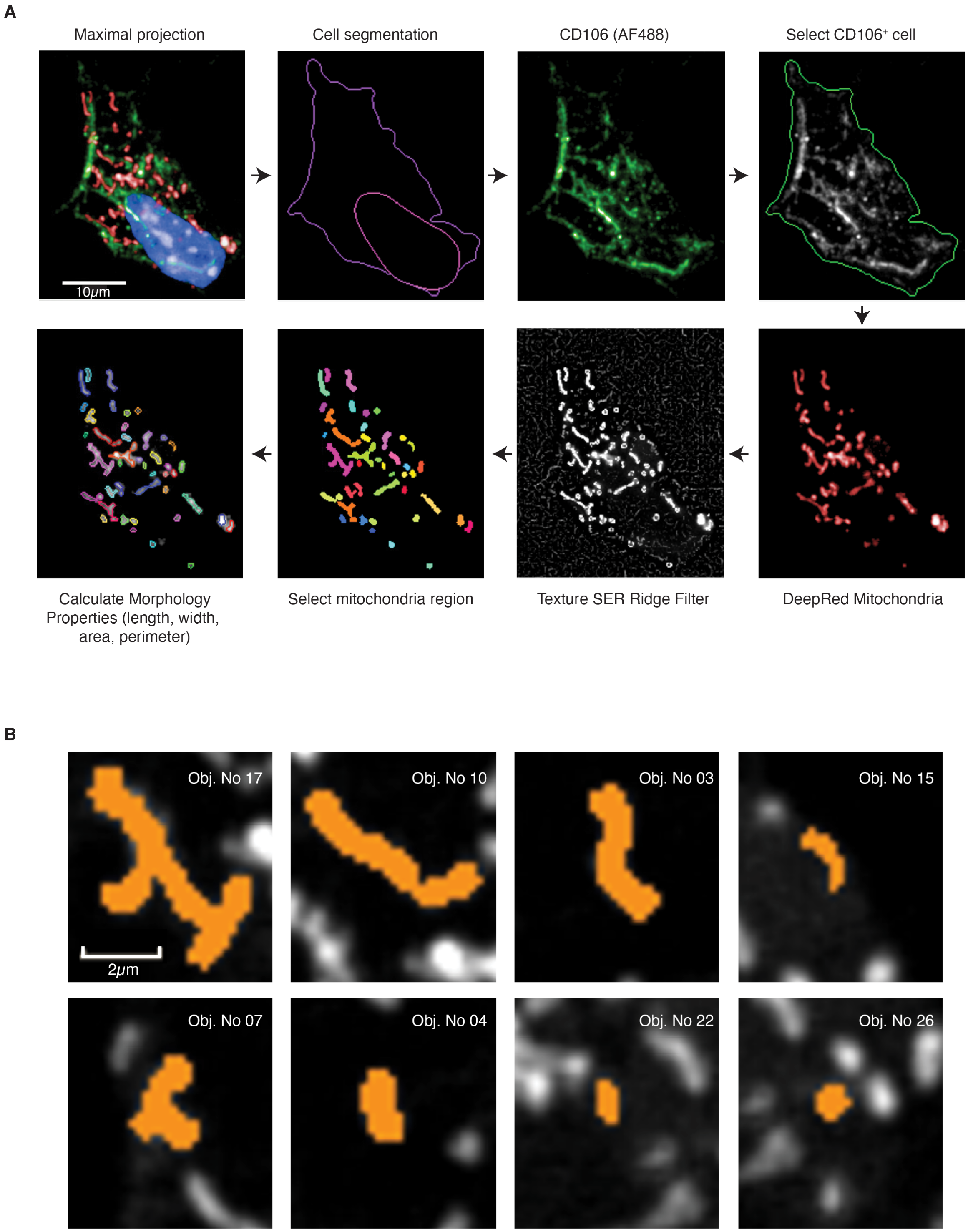

Object No	17	10	03	15	07	04	22	26
Form Factor	3.17	1.98	1.43	1.12	1.22	0.92	0.71	0.53
Aspect Ratio	6.90	6.48	4.67	3.02	2.70	2.20	1.90	1.03

Figure S3. Quantitation of mitochondrial morphology.

(**A**) Mouse embryonic heart single cells stained with MitoTracker Deep Red (MTDR), anti-CD106 (AF488) and DAPI were imaged by confocal microscopy. Maximal projection images (Z-stacks from 0 to 3 μm with a step size of 1 μm) were segmented to identify location of cells and nuclei. CD106$^+$ cells (cardiomyocytes) were selected for further analysis. The mitochondrial network was identified using the MTDR signal (mitochondria) transformed into Ridge texture using the SER (Saddles, Edges, Ridges) feature of Harmony. Mitochondrial network morphology was assessed by measuring the aspect ratio (major axis length/minor axis length) and form factor (perimeter^2/4π[area]), which are measures of distortion from circularity and degree of branching, respectively. (**B**) Eight example images of mitochondria (objects, Obj.) showing their aspect ratios and form factors.

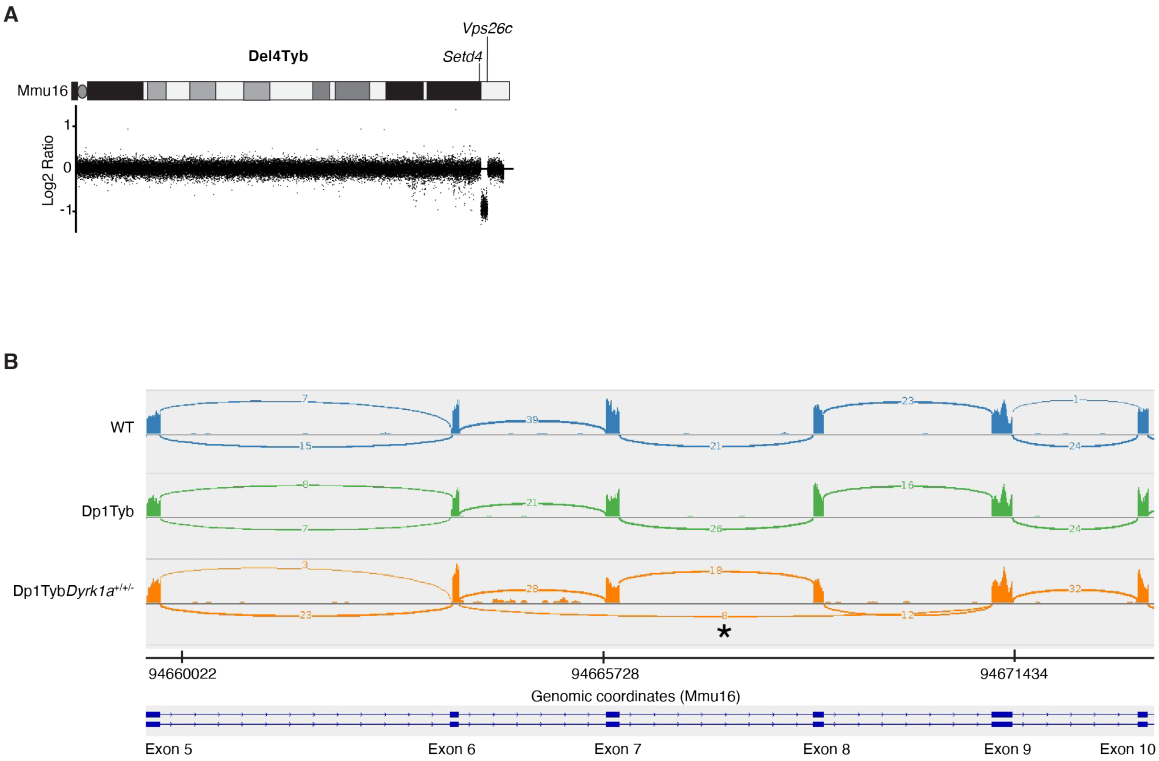

Figure S4. Validation of the Del4Tyb and Dp1Tyb*Dyrk1a*$^{+/+/-}$ mouse strains.

(**A**) Comparative genome hybridization analysis of the Del4Tyb mouse strain. Graph shows the log$_2$(ratio) of the hybridization signal between Del4Tyb and C57BL/6J control mice. Each dot is a different probe along the length of Mmu16, in genomic order. Diagram at top shows a map of Mmu16 indicating the acrocentric centromere and the location of the *Setd4* and *Vps26c* genes marking the ends of the deletion. The deleted region is expected to have 0.5-fold decrease in DNA content, resulting in a log$_2$(ratio) = -1. (**B**) Plot showing RNAseq reads mapped against the mouse genome within the *Dyrk1a* gene (exons 5 to 10) for E13.5 hearts from a WT, Dp1Tyb and Dp1Tyb*Dyrk1a*$^{+/+/-}$ embryo. Reads can be seen mapping against each exon and arcs indicate reads spanning introns. Numbers on the arcs show the numbers of reads showing the given splicing event. The Dp1Tyb*Dyrk1a*$^{+/+/-}$ embryo shows some reads connecting exon 6 to exon 9 (asterisk), as would be predicted if exons 7 and 8 had been deleted in one *Dyrk1a* allele. These connecting reads are not seen in WT or Dp1Tyb mice, confirming successful deletion of exons 7 and 8 in Dp1Tyb*Dyrk1a*$^{+/+/-}$ embryos.

A

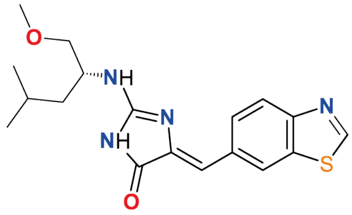

Leucettinib-21
IC$_{50}$ (DYRK1A): 3.1 nM

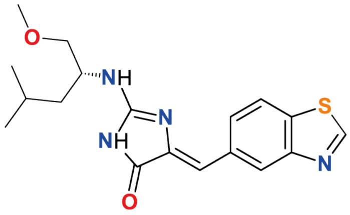

iso-Leucettinib-21
IC$_{50}$ (DYRK1A): >10 μM

B

Oral dose LCTB-21 (mg/kg)	LCTB-21 in embryo (ng/g)
0.3	ND
3	8.7±0.8
30	200.5±7.2

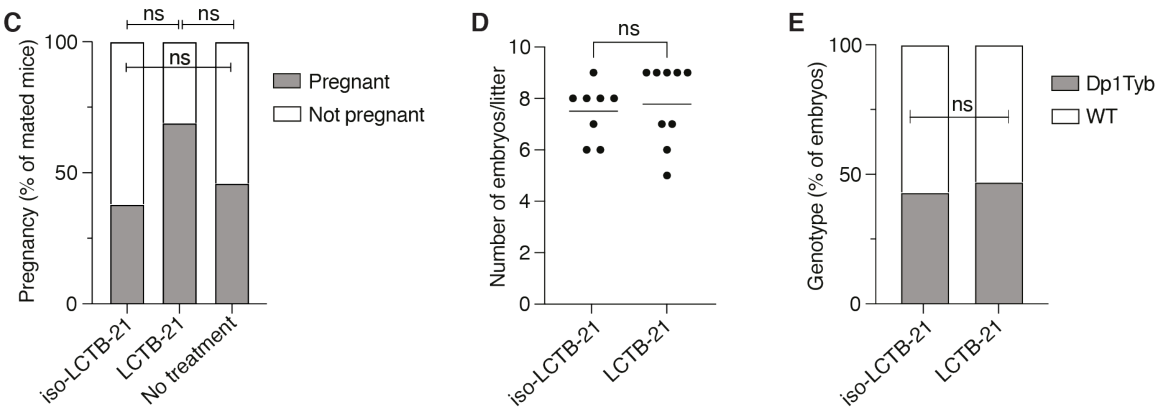

Figure S5. Treatment of pregnant mice with Leucettinib-21.

(A) Chemical structure of Leucettinib-21 (LCTB-21) and iso-Leucettinib-21 (iso-LCTB-21) indicating IC$_{50}$ concentrations for the inhibition of DYRK1A in vitro (LCTB-21 is compound 106 in *24*). (**B**) Pregnant C57BL/6J mice were treated with the indicated dose of LCTB-21 daily by oral gavage from E5.5 to E14.5 and embryos analyzed for abundance of LCTB-21 by mass spectrometry, with values listed as mean (±SEM) ng of LCTB-21 per g of embryo tissue. ND, not detected. (**C-E**) C57BL/6J female mice that had successfully mated with Dp1Tyb male mice as judged by the presence of a vaginal plug on the day following mating (embryonic day 0.5, E0.5) were treated daily with LCTB-21 or iso-LCTB-21 by oral gavage from E5.5 to E14.5 (Fig. 8A). Graphs show percentage of mated mice that (C) were pregnant at E14.5, (D) number of embryos per litter and (E) percentage of embryos whose genotype was WT or Dp1Tyb. Statistical analysis using Fishers exact (C, E) and Mann Whitney (D) tests; ns, not significant (P>0.05). Sample numbers: B, n=8 (0.3 or 3 mg/kg) and 4 (30 mg/kg) embryos; C, n=30 (iso-LCTB-21), 19 (LCTB-21) and 24 (no treatment) mice; D, n=8 (iso-LCTB-21) and 9 (LCTB-21) litters; E, n=60 (iso-LCTB-21) and 70 (LCTB-21) embryos.

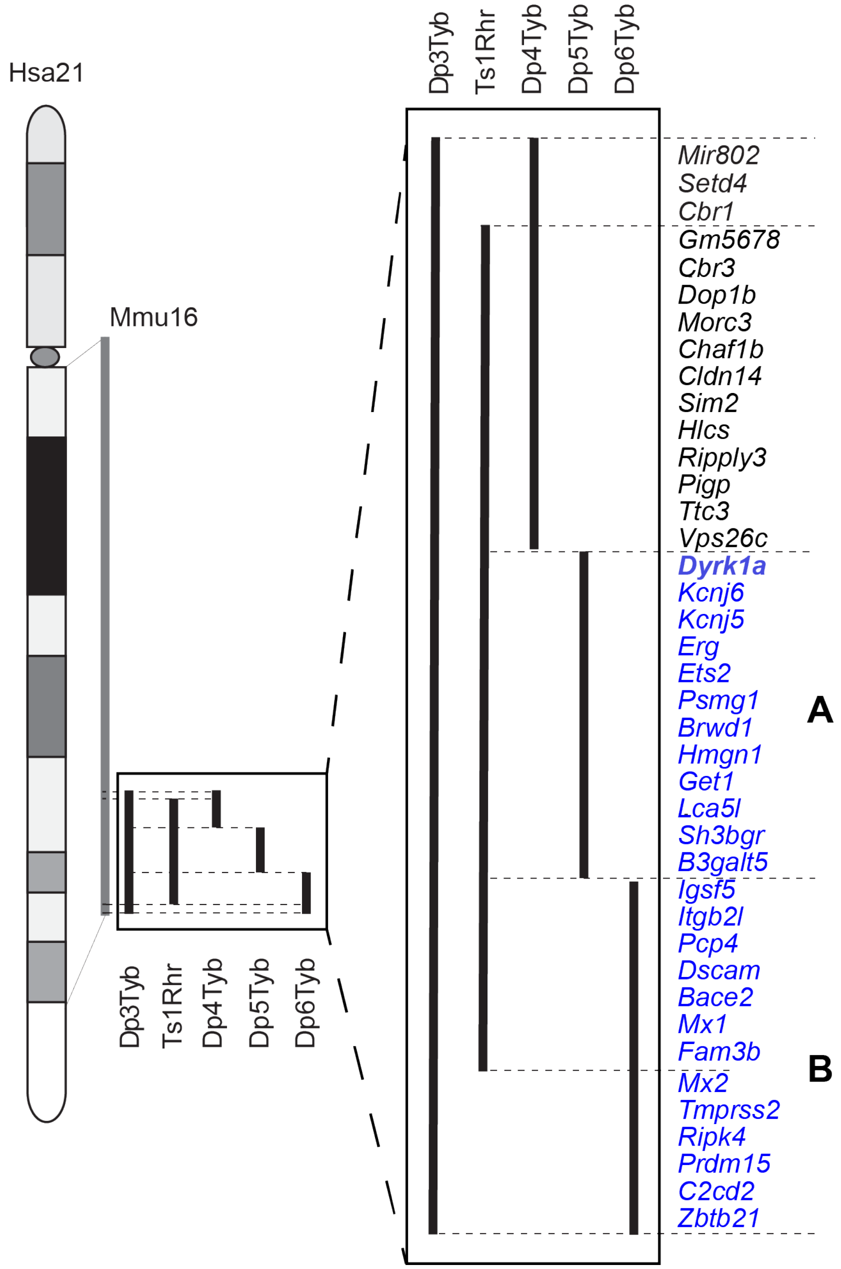

Figure S6. Regions of Hsa21 containing dosage-sensitive genes causing CHD.

Diagram of Hsa21 showing main cytogenic regions (rectangles of different shades) and the centromere (oval). Grey bar indicates the Hsa21-orthologous region of Mmu16. Black lines indicate regions of Mmu16 duplicated in the Dp3Tyb, Ts1Rhr, Dp4Tyb, Dp5Tyb and Dp6Tyb mouse strains. These regions are expanded showing all known protein coding genes within them and one microRNA gene (*Mir802*). Dp3Tyb mice have CHD, but

Ts1Rhr, Dp4Tyb, Dp5Tyb and Dp6Tyb do not, implying that there must be at least two causative genes. The genes in the Dp4Tyb region are not required for CHD, since a cross of Del4Tyb to Dp1Tyb did not affect the frequency of CHD. This implies that the two causative genes must lie in the regions duplicated in Dp5Tyb and Dp6Tyb respectively (regions A and B, genes in blue). We term this the 2-locus hypothesis. The *Dyrk1a* gene (bold) is required in three copies for the CHD phenotype, but there may be other genes in region A that are also required. The second unknown gene (*GeneX*) lies in region B and is most likely one of the 6 distal genes present in 3 copies in Dp3Tyb but not Ts1Rhr mice (*Mx2*-*Zbtb21*). Genes in regions that do not cause CHD are in black.

Supplementary Tables

Table S1. Human fetal hearts used for RNAseq analysis.

List of 10 human fetal heart samples obtained from HDBR (5 DS, 5 euploid) which were used for RNAseq showing gestational age and sex.

Table S2. RNAseq analysis of human Down Syndrome fetal hearts.

Sheet 1: Read me. Sheet 2: Expression of all genes in all samples in transcripts per million reads (TPM), and mean expression in each of the two genotypes (DS and euploid). Sheet 3: Differential gene expression analysis from DESeq2 showing for each gene its location, mean expression across all samples, log2(fold change) between DS and euploid and the *P*-value and adjusted *P*-value for this difference.

Table S3. RNAseq analysis of Dp1Tyb E13.5 mouse embryonic hearts.

Sheet 1: Read me. Sheet 2: Expression of all genes in all samples in transcripts per million reads (TPM), and mean expression in each of the two genotypes (Dp1Tyb and WT). Sheet 3: Differential gene expression analysis from DESeq2 showing for each gene its location, mean expression across all samples, log2(fold change) between Dp1Tyb and WT and the *P*-value and adjusted *P*-value for this difference.

Table S4. **RNAseq analysis of Dp3Tyb E13.5 mouse embryonic hearts.**

Sheet 1: Read me. Sheet 2: Expression of all genes in all samples in transcripts per million reads (TPM), and mean expression in each of the two genotypes (Dp3Tyb and WT). Sheet 3: Differential gene expression analysis from DESeq2 showing for each gene its location, mean expression across all samples, log2(fold change) between Dp3Tyb and WT and the *P*-value and adjusted *P*-value for this difference.

Table S5. **RNAseq analysis of Ts1Rhr E13.5 mouse embryonic hearts.**

Sheet 1: Read me. Sheet 2: Expression of all genes in all samples in transcripts per million reads (TPM), and mean expression in each of the two genotypes (Ts1Rhr and WT). Sheet 3: Differential gene expression analysis from DESeq2 showing for each gene its location, mean expression across all samples, log2(fold change) between Ts1Rhr and WT and the *P*-value and adjusted *P*-value for this difference.

Table S6. Expression of E2F targets and Hypoxia gene sets

Gene set enrichment analysis (GSEA) of the Hallmark gene set of E2F targets and Hypoxia gene sets. Sheet 1: Read me. Sheet 2: GSEA of E2F target genes in the comparison of transcriptomes of human DS and euploid fetal hearts, identifying genes in the leading edge. Sheet 3: GSEA of E2F target genes in the comparison of transcriptomes of Dp1Tyb and WT mouse embryonic hearts, identifying genes in the leading edge. Sheet 4: GSEA of E2F target genes in the comparison of transcriptomes of Dp1Tyb*Dyrk1a*$^{+/+/-}$ and WT embryonic hearts, identifying genes in the leading edge. Sheet 5: Comparison of the leading genes in the GSEA of E2F target genes of human DS v euploid and mouse Dp1Tyb v WT embryonic hearts. Sheet 6: GSEA of Hypoxia genes in the comparison of transcriptomes of Dp1Tyb and WT embryonic hearts.

Table S7. RNAseq analysis of Dp1Tyb*Dyrk1a*$^{+/+/-}$ E13.5 mouse embryonic hearts.

Sheet 1: Read me. Sheet 2: Expression of all genes in all samples in transcripts per million reads (TPM), and mean expression in each of the two genotypes (Dp1Tyb*Dyrk1a*$^{+/+/-}$ and WT). Sheet 3: Differential gene expression analysis from DESeq2 showing for each gene its location, mean expression across all samples, log2(fold change) between Dp1Tyb*Dyrk1a*$^{+/+/-}$ and WT and the *P*-value and adjusted *P*-value for this difference.

Table S8. Proteomic analysis of Dp1Tyb*Dyrk1a*$^{+/+/-}$ E13.5 mouse embryonic hearts.

Sheet 1: Read me. Sheet 2: Abundance of phospho-peptides in all samples, the Welch difference, a measure of fold-change between Dp1Tyb*Dyrk1a*$^{+/+/-}$ and Dp1Tyb hearts (log2[fold change of the geometric means]), and the *P*-value. Sheet 3: Abundance of peptides in all samples, the log2(fold change) between Dp1Tyb*Dyrk1a*$^{+/+/-}$ and Dp1Tyb hearts, and the FDR-adjusted *P*-value.

Table S9. Effect of Dyrk1a dosage on differential gene expression.

Sheet 1: Read me. Sheet 2: DESeq2 analysis of the transcriptomes of Dp1Tyb v WT embryonic hearts. Sheet 3: DESeq2 analysis of the transcriptomes of Dp1Tyb v Dp1Tyb*Dyrk1a*$^{+/+/-}$ embryonic hearts. Sheet 4: Differentially expressed genes in common between those identified in sheets 2 and 3. Sheet 5: STRING analysis of the common upregulated genes. Sheet 6: STRING analysis of the common downregulated genes. Sheet 7: Genes and proteins upregulated and downregulated in RNAseq or proteomic analysis of Dp1Tyb v Dp1Tyb*Dyrk1a*$^{+/+/-}$ embryonic hearts, indicating genes/proteins in common between the two analyses.

Table S10. RNAseq of Dp1Tyb and WT embryonic hearts from pregnant mice treated with Leucettinib-21 or iso-Leucettinib-21.

Sheet 1: Read me. Sheet 2: Normalized counts of all genes in all samples, and mean expression for each condition. Sheet 3: Differential gene expression analysis from DESeq2 showing for each gene its location, mean expression across all samples, log2(fold change) between Dp1Tyb embryonic hearts treated with iso-Leucettinib-21 and WT embryonic hearts treated with iso-Leucettinib-21, the *P*-value and an indication if the adjusted *P*-value reached significance. Sheet 4: Differential gene expression analysis from DESeq2 showing for each gene its location, mean expression across all samples, log2(fold change) between Dp1Tyb embryonic hearts treated with Leucettinib-21 and WT embryonic hearts treated with iso-Leucettinib-21, the *P*-value and an indication if the adjusted *P*-value reached significance.